MAFIC EXPLOSIVE VOLCANISM AT LLAIMA VOLCANO: 3D X-RAY MICROTOMOGRAPHY RECONSTRUCTION OF PYROCLASTS TO CONSTRAIN SHALLOW CONDUIT PROCESSES

by

Pedro Antonio Valdivia-Munoz

A thesis

submitted in partial fulfillment

of the requirements for the degree of

Master of Science in Geoscience

Boise State University

August 2021

BOISE STATE UNIVERSITY GRADUATE COLLEGE

DEFENSE COMMITTEE AND FINAL READING APPROVALS

of the thesis submitted by

Pedro Antonio Valdivia-Munoz

Thesis Title: Mafic Explosive Volcanism at Llaima Volcano: 3D X-ray Microtomography Reconstruction Of Pyroclasts to Constrain Shallow Conduit Processes

Date of Final Oral Examination: 03 May 2021

The following individuals read and discussed the thesis submitted by student Pedro Antonio Valdivia-Munoz, and they evaluated their presentation and response to questions during the final oral examination. They found that the student passed the final oral examination.

Brittany Brand, Ph.D.	Chair, Supervisory Committee
Michael Manga, Ph.D.	Member, Supervisory Committee
Dorsey Wanless, Ph.D.	Member, Supervisory Committee

The final reading approval of the thesis was granted by Brittany Brand, Ph.D., Chair of the Supervisory Committee. The thesis was approved by the Graduate College.

DEDICATION

This thesis is dedicated to my family and wife. For their unconditional support and love.

ACKNOWLEDGMENTS

I would like to sincerely thank my supervisor, Dr. Brittany Brand, for her guidance and constant support, and specially for her confidence in me. I would also like to thank Dr. Michael Manga for serving as a member of my committee. I learned so much from him. To Aaron Marshal, Sean Carney, Jade Bowers, Dorsey Wanless, Guido Giordano, Ben Andrews, Alessandro Vona and Madison Myers for a wonderful fieldtrip in Chile and further support. To all the professors and graduate students I met during my two years living in Boise, thank you very much.

To all my friends and family, thank you for your constant support and love. And specially to my wife, Lara Leiss, my favorite person in this world. Your love and company are the most unvaluable treasures I have.

This work was funded by the NSF award # 1831143, so thanks to Dr. Brand for letting me be part of the “Llaima team”.

ABSTRACT

Mafic eruptions, which are typically effusive to mildly explosive, can produce much stronger explosive eruptions. Eruption style is determined by the ability of gas to escape through the permeable network. If the permeability is sufficiently high to reduce vesicle overpressure during ascent, the volatiles may escape from the magma, inhibiting violent explosive activity. In contrast, if the permeability is sufficiently low to retain the gas phase within the magma during ascent, bubble overpressure may drive magma fragmentation. Rapid ascent rates may induce disequilibrium crystallization, increasing viscosity and explosivity, and have consequences for the geometry of the vesicle network. Quantitative vesicle texture analyses are commonly measured in 2D. However, 2D vesicle analyses do not provide sufficient information about the internal vesicle structures for permeability analysis. Here we use synchrotron X-ray computed microtomography of 10 pyroclasts from the 12.6 ka mafic Curacautín Ignimbrite (Llaima Volcano, Chile) to reconstruct and quantify pyroclast textures in three dimensions. Our goal is to obtain 3D measurements of porosity, bubble interconnectivity, bubble number density, and geometrical properties of the porous media to investigate the role of magma degassing processes at mafic explosive eruptions. We use an analytical technique to estimate permeability and tortuosity by combing empirical relationships and pyroclasts vesicle textures. We identified two populations of vesicles: (1) a convoluted connected vesicle network produced by extensive coalescence of smaller vesicles (>99% of pore space), and (2) a population of very small and completely isolated vesicles (<1% of porosity network).

Bubble numbe2r density measurements are 1-29×10^3 bubbles per mm^3, implying an average decompression rate of 1.4 MPa/s under heterogeneous nucleation. We computed tortuosities factor between 1.89 and 4.4, with higher values in the less vesicular samples. Permeability ranges are between 3×10^{-13} and 6.27×10^{-12} m^2. 3D vesicle textures evidence rapid ascent rates that induced high disequilibrium, promoting rapid syn-eruptive crystallization of microlites and late vesiculation. We propose that the increase in viscosity due to crystallization and vesiculation, combined with rapid ascent, inhibited outgassing and increased bubble overpressures, leading to explosive fragmentation. We estimated that a bubble overpressure greater than 5.2 MPa could have been sufficient to fragment the Curacautín magma. Other mafic explosive eruptions report similar disequilibrium conditions induced by rapid ascent rate, implying that syn-eruptive disequilibrium may control the explosivity of mafic eruptions more generally.

TABLE OF CONTENTS

LIST OF TABLES

LIST OF FIGURES

LIST OF ABBREVIATIONS

2D	2-dimentional
3D	3-dimentional
BSU	Boise State University
BND	Bubble Number Density
FO	Forcheimer Number
GC	Graduate College
ID	Identification
MATLAB	Matrix Laboratory
MSH	Mount Saint Helens
SEM	Scanning Electron Microscopy
ST	Stokes Number
TDC	Thesis and Dissertation Coordinator
VOI	Volume of Interest

CHAPTER ONE: INTRODUCTION

Mafic eruptions, which are typically effusive to mildly explosive, are the most common style of volcanism on Earth (Parfitt, 2004). However, mafic volcanoes can produce much stronger, Plinian-style eruptions, capable of destructive pyroclastic currents and widespread ash fall (La Spina et al., 2020). The most powerful examples include the basaltic Plinian deposits of ~60 ka Fontana Lapilli and ~2 ka Masaya Triple Layer at Masaya volcano in Nicaragua (Constantini et al., 2009; Constantini et al., 2010; Bamber et al., 2020; Pérez et al., 2020); the 122 BC eruption of Etna, Italy (Coltelli et al., 1998; Houghton et al., 2004; Sable et al., 2006); and the 1886 Tarawera eruption, New Zealand (Houghton et al., 2004; Sable et al., 2006; Shea et al., 2017; Moitra et al., 2018).

In general, explosive eruptions are modulated by the conditions of volatile exsolution that lead to vesiculation. Vesiculation is a process in which volatiles originally dissolved in the magma exsolve into gas bubbles due to a decrease in the pressure-dependent solubility during magma ascent (Yoshimura, 2019). The resulting bubbles undergo decompression expansion, reducing the bulk mixture density of the magma and enhancing buoyancy (Cassidy et al., 2018). As bubbles expand, they coalesce to form permeable pathways connecting the dispersed volatile phase (Klug and Cashman, 1996). If the resulting permeability is sufficiently high to reduce vesicle overpressure during ascent, the volatiles may escape from the magma, limiting the chance of violent explosive activity. In contrast, if the permeability is sufficiently low to maintain the gas phase trapped within the magma during ascent, overpressure in bubbles may drive magma fragmentation,

producing an explosive eruption (Mueller et al., 2008; Degruyter at al., 2012; Cashman and Scheu, 2015; Cassidy et al., 2018). The exsolution of volatiles within a magma is controlled by decompression rate, the degree of volatile saturation, availability of nucleation sites, surface tension, and viscosity of magma (Mangan et al., 2004; Cassidy et al., 2018).

Many studies show that there is a link between mafic explosive volcanism, rapid ascent, and syn-eruptive disequilibrium conditions in both the gas and solid phases (La Spina et al., 2016; Polacci et al., 2018; Arzilli et al., 2019; Bamber et al., 2020; Namiki et al., 2021). When decompression rate is high, the volatiles may not degas from the magma under equilibrium conditions. Such disequilibrium degassing may lead to volatile supersaturation, late vesiculation, and high bubble overpressures (Mangan and Sisson, 2000). Similarly, crystallization kinetics are controlled by water content, degassing, and ascent rates (La Spina et al., 2016; Befus and Andrews, 2018; Arzilli et al., 2019). High degrees of disequilibrium due to rapid ascent results in high crystal nucleation and growth rates (Befus and Andrews, 2018). This increases the magma bulk viscosity and may further prevent degassing, promoting the conditions necessary for explosive volcanism (Arzilli et al., 2019).

The volatile and crystal textures of magmas are critical in determining their rheology and eruptive behavior (Gonnermann and Manga, 2007). Rapid crystallization due to disequilibrium degassing triggers profound rheological changes in ascending magmas (Vona et al., 2011; Arzilli et al., 2019). Indeed, pyroclasts from mafic Plinian eruptions typically display high microlite number densities (Murch and Cole, 2019), suggesting that changes in rheology due to rapid crystallization may be responsible for triggering highly explosive basaltic volcanism (Sable et al., 2006).

Pyroclasts from explosive eruptions record the state of the volatile phase in the conduit prior fragmentation (Degruyter et al., 2010). Thus, pyroclasts vesicle textures can be used to constrain magma permeability at the time of fragmentation, as well as ascent rate and fragmentation conditions (Mueller et al., 2005; Toramaru, 2006; Polacci et al., 2010). The most common approach to investigate vesicle texture is using 2D images via scanning electron microprobe (SEM) on thin sections. However, this technique does not provide sufficient information about the internal vesicle structures in 3D for permeability analysis (Polacci et al., 2010; Giachetti et al., 2011). Even with 3D analysis, permeability and tortuosity estimates often require lab measurements or numerical modeling, which may not be an option due to pyroclast size (too small for lab permeameters) and computational challenges to simulate a large enough volume to be representative.

The objective of this study is to use 3D X-ray microtomography reconstructions of pyroclasts to measure porosities, bubble number density, vesicle interconnectivity and geometrical properties of the porous media. We then develop an analytical technique to estimate permeability and tortuosity by combing empirical relationships and pyroclasts vesicle textures.

We focus on pyroclasts produced by the large volume 12.6 ka mafic explosive eruption of Llaima volcano (38°41’45 S, 71°43’54 W), responsible for the extensive Curacautín Ignimbrite (Fig. 1; Naranjo and Moreno, 1991; Marshall et al., in prep). The Curacautín Ignimbrite is a massive, poorly sorted, and matrix-supported lapilli tuff. The eruption produced four flow units of variable thickness with SiO_2 content between 53 and 54.51 wt.% (Marshall et al., in prep). We collected samples stratigraphically (Units 1 – 4) from the most complete exposure, which is located southeast from the summit (Fig. 1).

Previous work shows that Curacautín pyroclasts are lapilli size, subrounded, micro-vesicular with low phenocrysts contents (2-3%; Lohmar, 2008), but are rich in plagioclase microlites (7.95-18.4×10^6 per mm^3. Fig. 2; Marshal et al., in prep). 2D analyses suggest that vesicles shapes are controlled by an abundance of plagioclase microlites (Martel and Iacono-marziano, 2015).

Here we report 3D results using X-ray microtomography of porosity, bubble number density, surface areas, tortuosity, and permeability of pyroclast from the Curacautín Ignimbrite. We then estimate decompression rates, the degree of coupling between the gas phase and the magma, and the evolution of vesiculation during ascent to investigate the role of magma degassing processes at mafic explosive eruptions. Finally, we discuss the consequences of disequilibrium conditions and compare our results with other basaltic explosive eruptions.

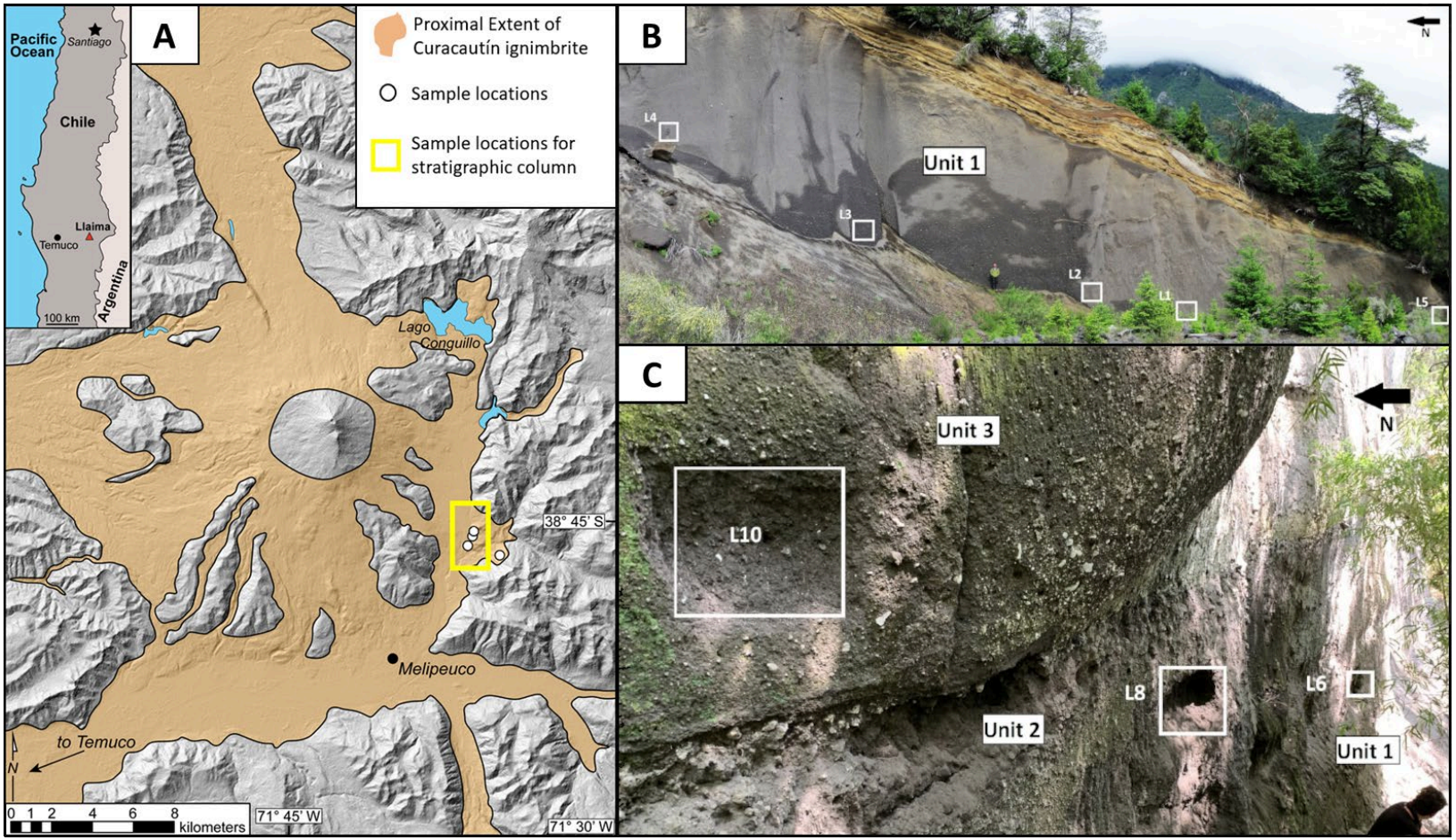

Figure 1 (A) Map showing Curacautín deposits and sample locations (southeast of Llaima volcano summit). (B) Photo of Unit 1, the thickest deposit in the sequence. The base is not exposed. (C) Photo showing the contact between Unit 1, Unit 2, and Unit 3. Samples L12 (top of Unit 1) and L18 (Unit 4) are not visible in these photos. Modified from Marshall et al., in prep.

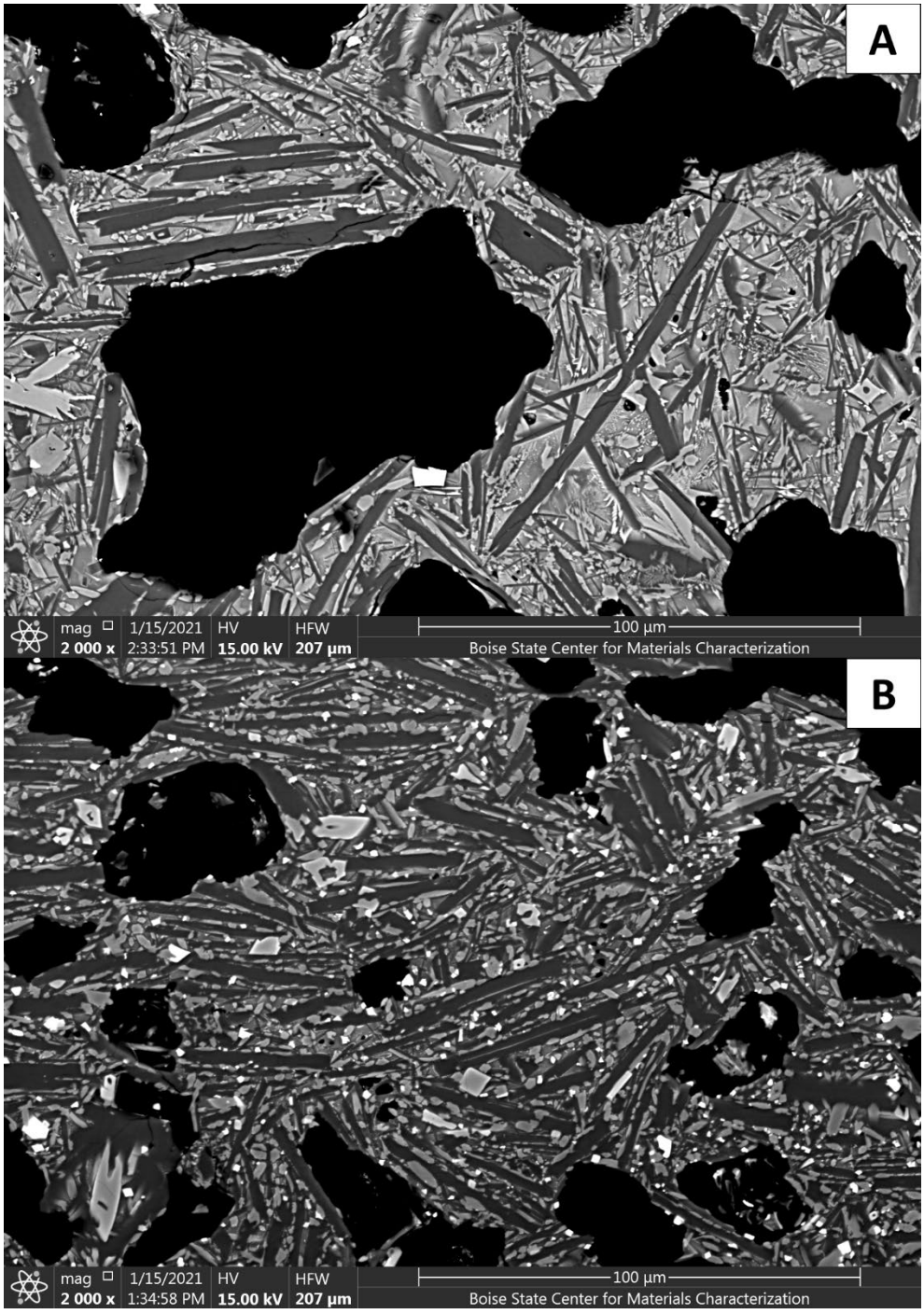

Figure 2 SEM image of a pyroclast from the Curacautín Ignimbrite. (A) Sample L1, Unit 1. (B) Sample L8, Unit 2. The vesicle shapes are controlled by the high amount of plagioclase microlites.

CHAPTER TWO: METHODOLOGY

Sample Preparation

Collected pyroclasts were picked, cleaned, and sorted by density (Table 1; Marshall et al., in prep.). We chose the mean and median density pyroclasts from each sample for 3D analysis and drilled 3.4 mm diameter cores for further X-Ray microtomography. The mean pyroclast density for each sample was chosen for this study; if the mean pyroclast was unavailable, we used the median density pyroclast for 3D analysis. Cores were immersed in an ultrasonicator water bath for 25 minutes to remove powder produced by coring, then dried in an oven at 95 ˚C.

X-ray microtomography

X-Ray microtomography was performed on beamline 8.3.2 at the Advanced Light Source, Lawrence Berkeley National Lab. 2D images were acquired over five sessions between September 2017 and October 2018. Owing to differences in beam stability and small changes in setup, scanning parameters varied slightly between sessions to optimize image quality. Images were acquired with 25-30 keV monochromatic X-rays and 200 millisecond exposure times. 1025-2625 projections were imaged with a PCO edge camera, a 5X Mitutoyo lens, and a 50 mm LuAG scintillator over a 180 degrees continuous rotation of the sample. Isotropic pixel size was 1.3 microns. A subset of 5 samples were imaged 0.64 microns/pixel for comparison. Image reconstruction was performed with Xi-cam (Pandolfi et al., 2018), including center of rotation optimization along with ring and outlier removal.

3D reconstruction

Image processing, volume rendering, and geometric computations were generated using the Dragonfly software, Version 2020.1.0.797 for Windows 10 (Object Research Systems (ORS) Inc, Montreal, Canada, 2018; software available at http://www.theobjects.com/dragonfly). All 2D and 3D images were extracted using the Dragonfly software. We stacked 820 2D images per sample to reconstruct the 3D microstructures. Due to the size of the resulting volume (22.2 GBs; Fig. 3A) and the computational problems to process that amount of data, four cubic sub volumes of 820x820x820 pixels (~1.21 mm^3) per sample were extracted as Volumes of Interest (VOI; Figure 3C). These VOIs are large enough to be representative of the complexity and heterogeneity of the samples, but small enough to not overwhelm the computing resources available for this project (Baker et al., 2012; Degruyter et al., 2010). We selected four sub volume locations vertically throughout each core sample to reduce ring errors (maximum at the center of the sample) and avoid the cylindrical boundaries of the 2D images (Fig. 3A, Fig. 3B). Using four VOIs also provides a sensitivity analysis, enabling error calculations.

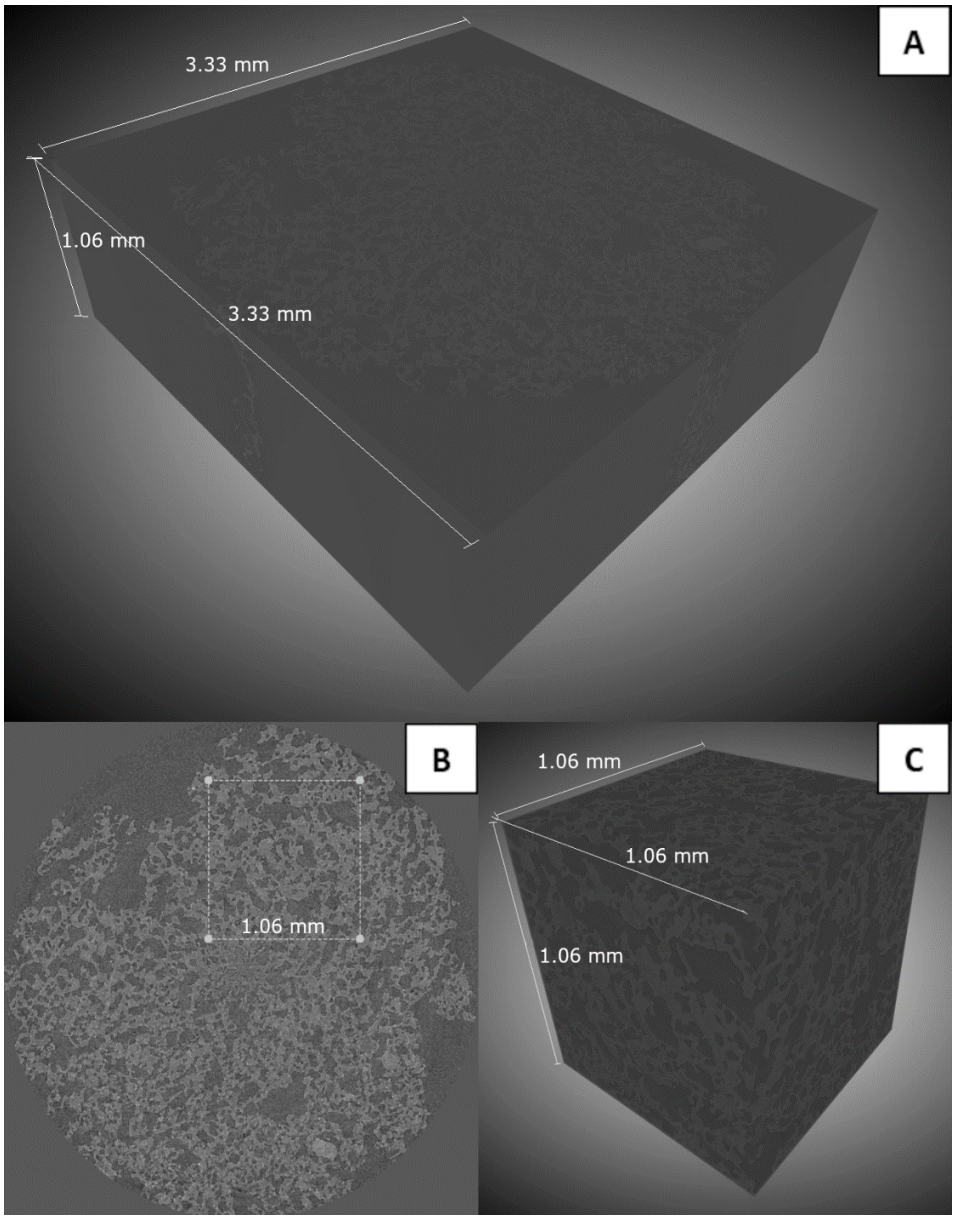

Figure 3 Image reconstructions and Volume of interest. (A) 3D reconstruction of L4. Image was obtained stacking 820 reconstructed 2D X-ray microtomography images (B) 2D orthogonal view from the top of the volume. The white dashed square represents the area of interest used to generate a subvolume (C) 3D visualization of sample L4(Figure 2), one of the four volumes of interest we extracted per sample.

In order to analyze and visualize the pore network, the VOIs were segmented using Dragonfly's segmentation toolkit. This process partitions the volume into groups of voxels of each phase of interest. For simplicity, we defined two phases of interest: pores and solid rock. We utilized a segmentation criteria based on a brightness/grayscale histogram

threshold, where the darker voxels correspond to bubbles or pores and the brighter ones correspond to the solid phase (Fig. 4A). Commonly, this process leads to the generation of artifacts and errors due to the heterogeneities in pixel brightness (Figure 4B; Baker et al., 2012; Degruyter et al., 2010; Ketcham and Carlson, 2001; Ketcham, 2005; Shanti et al., 2014). Thus, a cleaning procedure was performed using morphological operations, part of Dragonfly's segmentation toolkit, to "Erode", "Dilate" and "Smooth", effectively removing artifacts such as islands and holes smaller than 9 voxels. This process was repeated as many times as necessary until a clear, bimodal image was produced (confirmed by a visual inspection, Fig. 4C). Once the segmentation was successful, we separated the interconnected voxels from the isolated ones (Fig. 4D). Every connected or isolated pore was counted and identified, followed by the computation of geometrical properties as Volume and Surface Area (Appendix A.1).

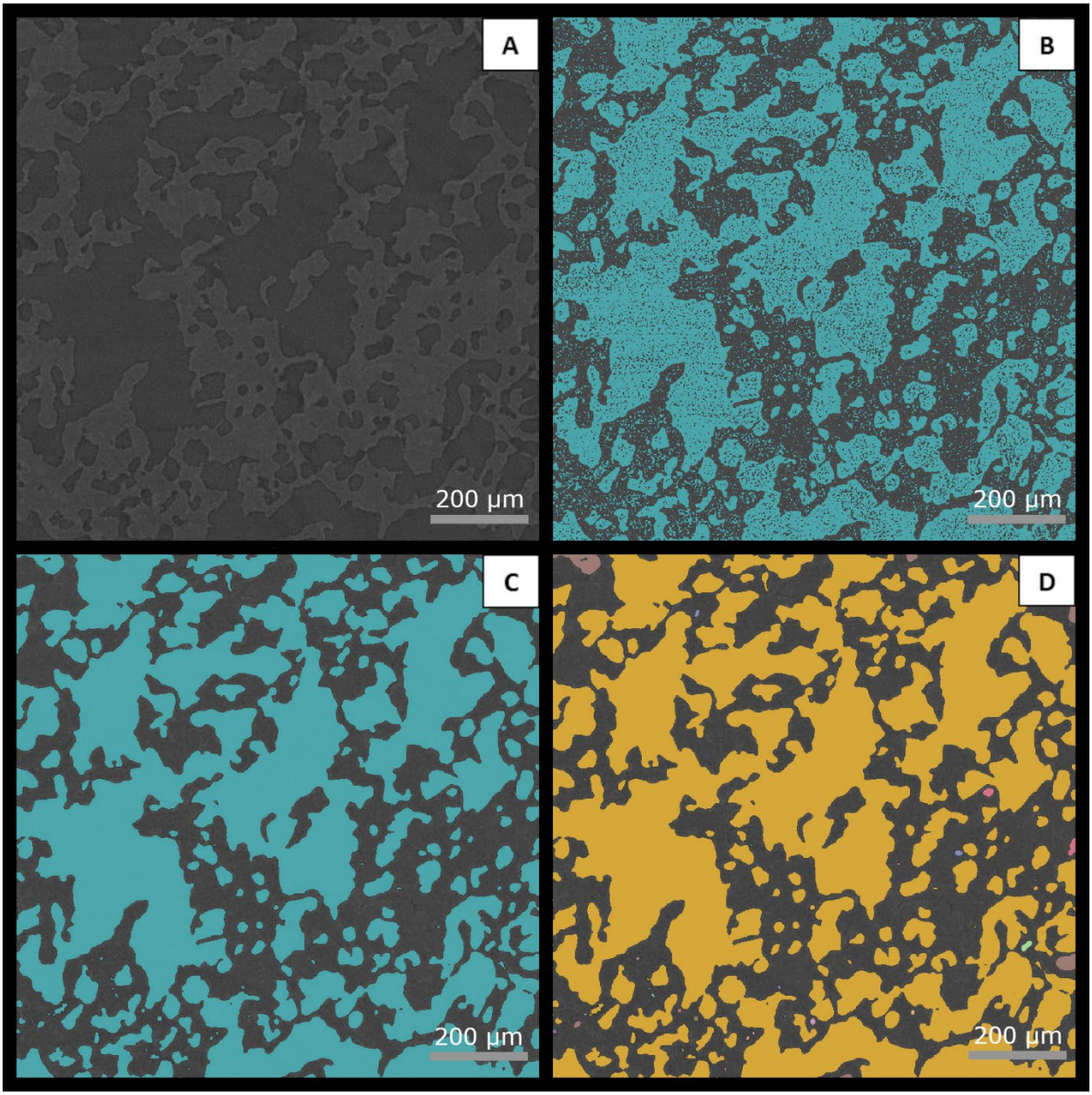

Figure 4 (A) 2D view of a slice of one VOI (sample L4). Darker grey pixels correspond to pores/vesicles, while the brighter ones correspond to the solid phase. (B) Segmentation based on a brightness/grayscale histogram threshold. The segmented phase in cyan color shows the artifacts in the form of islands and holes. (C) Final view of the cleaning process after using morphological operations as "Erode", "Dilate" and "Smooth" to remove artifacts shown in (B). (D) 2D view of the separation of vesicles. Every color represents a single vesicle. The golden color represents one single convoluted vesicle.

Quantification of 2D and 3D vesicle textures in terms of vesicularity (volumetric fraction of vesicles), bubble number densities (number of vesicles per unit volume), vesicle volume, surface areas, and connectivity (volume fraction of connected vesicles) were performed with the same software (Table 1, Appendix A.1). Additionally, we extracted 3D visualizations of the skeletonization (Fig. 5D), segmented phases (Fig. 5B), and separated phases (Fig. 5C). The final 3D segmented volumes were extracted as 2D 8-bit binary images for further tortuosity analysis.

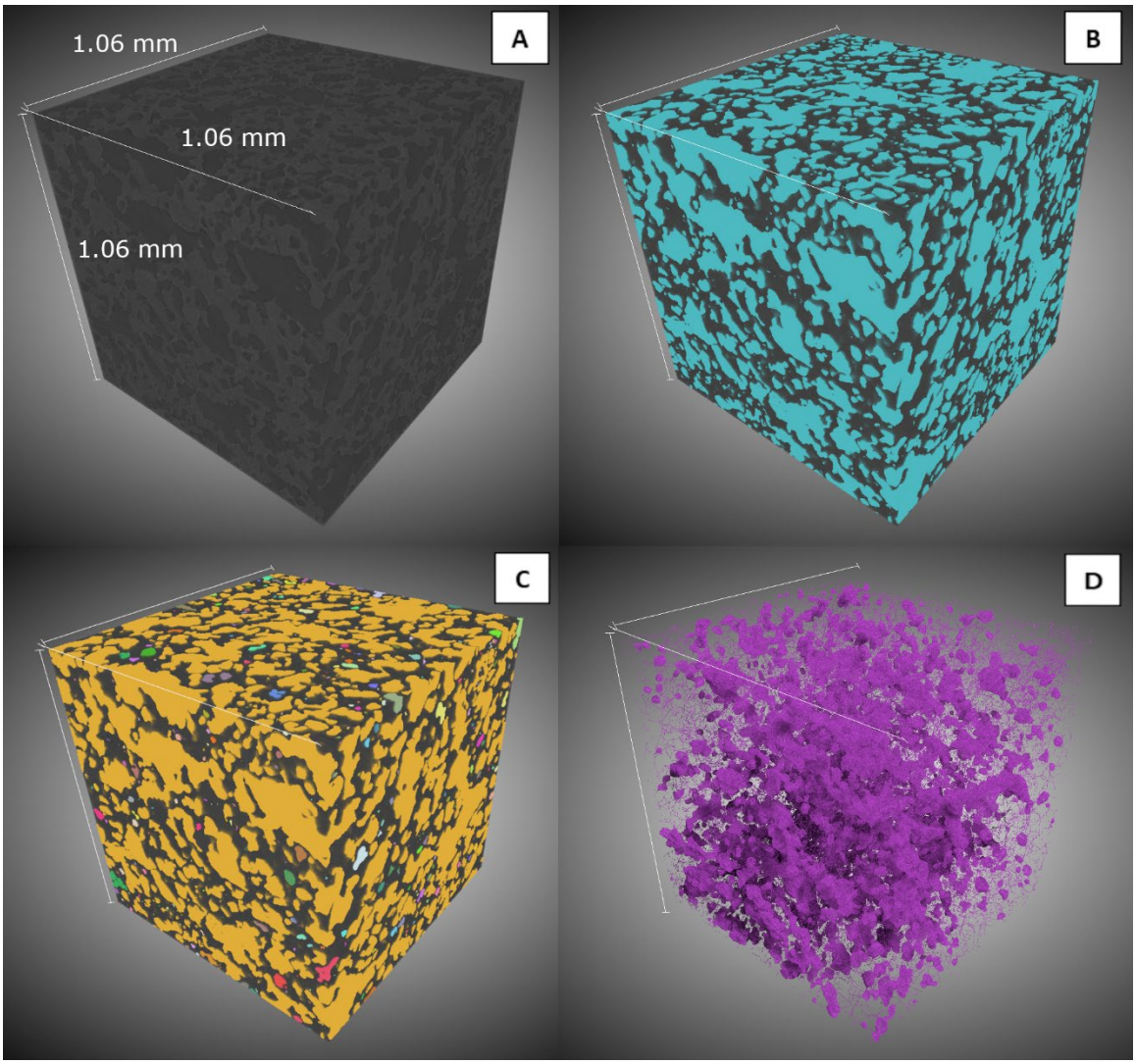

Figure 5 3D visualization of L4. All three volumes have the same size. (A) 3D reconstruction of L4. (B) Segmentation of the porous media represented in cyan color. (C) Separation of interconnected vesicles. Every color represents a single bubble. (D) 3D visualization of the skeletonization of sample L4. The purple matrix represents the medial axis of the pore network. The convoluted shape and the chaotic distribution of the final structure make it very difficult to calculate classic tortuosity.

3D Tortuosity factor

Tortuosity factors (τ^*) were calculated using the MatLab application TauFactor (Cooper et al., 2016). TauFactor calculates the changes in diffusive transport produced by convolutions and heterogeneities of the interconnected porous media (Eq. 1; Backeberg et al., 2017; Cooper et al., 2016). Equation (1) calculates effective diffusivity (D_{eff}) in terms of tortuosity factor,

$$D_{\text{eff}} = D_0 \frac{\epsilon}{\tau^*} \quad (1)$$

where D_0 is the intrinsic diffusivity of the conductive phase and ε is the volume fraction of the porous phase. TauFactor calculates the directional tortuosity factor along three mutually perpendicular axes of interconnected "diffusive phases" (or porous phases) through a 3D volume generated by stacking binary or trinary 2D images (Appendix A.3)

It is important to note that tortuosity factor and tortuosity (τ) are two different parameters, although both characterize the relationship between the geometry and length of interconnected phases. In porous media, tortuosity is defined as the ratio between the flow-path length and a straight line length in the direction of flow, which has been commonly used to quantify flow, or diffusion along porous media (Suman and Ruth, 1993; Shanti et al., 2014; Backeberg et al., 2017; Cooper et al., 2016). Tortuosity is measured from skeletonized data using finite element analysis or finite difference calculation on meshed data (Shanti et al., 2014). Unfortunately, the skeletonization of the porous network of our samples are too complex and chaotic for this kind of operation (Fig. 5D). As such, a tortuosity factor calculation is better suited for modelling more complex pore networks such as those in our clasts (Backeberg et al., 2017; Cooper et al., 2016).

In a system where the cross-sectional area of the flow path remains constant, tortuosity factor is equal to the square of tortuosity (Eq. 2; Tjaden et al., 2016; Backeberg et al., 2017).

$$\tau^* \simeq \tau^2 \quad (2)$$

The Tortuosity factor and tortuosity both increase as pathways become more contorted. Both parameters approach 1 when the cross-sectional area of the flow pathways remains constant and the direction of flow follows the axis that is orthogonal to that cross-sectional area (Backeberg et al., 2017).

TauFactor also computes 2D volume fractions, 3D phase volume fraction (vesicularity), effective diffusivity (D_{eff}), directional percolation, tortuosity factor (τ^*), and a provides a visual representation of the flux during steady state (Appendix A.3).

Permeability calculations

One of the most widely used relationships between permeability and tortuosity is the Kozeny-Carman relation (Yokoyama and Takeuchi, 2009; Matyka and Koza, 2001; Farquharson et al., 2015; Berg, 2014; Bernard et al., 2007; Wei et al., 2018)

$$k_1 = \frac{\phi^3}{c\tau^2 S^2} \quad (3)$$

where k_1 is the Darcian permeability, given by the porosity (ϕ), tortuosity (τ), the surface area per unit volume (S) and the Kozeny constant (c). Bernabe et al. (2010) defines two simplified Kozeny constants: a crack-controlled media where c = 12; and a pore-controlled media where c = 8 (Farquharson et al., 2015). We use c = 8 due to the nature of the porous network. Given the complexity of the porous media and the low variation in the cross-sectional area of the flow path, we combined Eq. (2) and Eq. (3) to find a relationship between permeability and tortuosity factor (Eq. 4):

$$k_1 \simeq \frac{\phi^3}{c\tau^* S^2} \quad (4)$$

Decompression and discharge rates

We use the bubble number density decompression rate meter proposed by Toramaru (2006) to calculate decompression rates (*dP/dt*) from volumetric bubble number densities (N_v) for basaltic magmas under heterogeneous nucleation (Eq. 5; Shea, 2017; Toramaru, 2006):

$$\frac{dP}{dt} = \left(\frac{N_v}{5(\pm 3.5)\times 10^3}\right)^{\frac{2}{3}} \quad (5)$$

Additionally, if we assume a cylindrical conduit geometry, we can estimate mass discharge rates ($\dot{m}$) as a function of bulk magma density (ρ_m), decompression rate, pressure gradient in the conduit (*dP/dz*), and conduit radius (*r*) (Shea, 2017):

$$\dot{m} = \rho_m \left(\frac{dP}{dz}\right)^{-1} \left(\frac{dP}{dt}\right) \pi r^2 \quad (6)$$

We approximate the pressure gradient in the conduit with the magmastatic gradient. For a mafic magma at 1200˚C, dP/dz = 0.026 MPa m^{-1} (Cas and Simmons, 2018). We used the bulk magma density (ρ_m) (i.e. melt +vesicles±crystals) as the average density of our pyroclasts for Unit 1, $\rho_{bulk} \sim 1290$ kg m^{-3}(Marshall et al., in prep.). For the radius, we considered that Plinian eruptions require larger conduits radius, between 10 and 150 m, to explain the relationship between mass discharge and decompression rates (Shea, 2017). As such, we calculated three discharge rates for radii of 25, 50 and 100 m.

Forchheimer and Stokes numbers

We calculated the Stokes and Forchheimer numbers for Unit 1 following Degruyter et al. (2012) equations to validate and compare our results with the Plinian phase of the May 18, 1980 eruption of Mount St. Helens (MSH 1980, Degruyter et al., 2012). The Stokes number (St) is a non-dimensional number that represents the ratio of the magma response time scale and the gas phase characteristic flow time (Eq. 7):

$$\mathrm{St} = \frac{\frac{\rho_m k_1}{\mu_g}}{\frac{r}{U_o}} \quad (7)$$

where ρ_m is the bulk magma density, k_1 is the Darcian permeability, μ_g is the viscosity of the gas phase, r is the conduit radius, and U_0 is the velocity. Velocity is calculated as the ratio between the mean decompression rate and the magmastatic gradient in the conduit. When St is small, magma and gas are coupled and ascend at the same velocity, preventing degassing. For larger St, the degree of coupling decreases inducing degassing (Degruyter et al., 2012; La Spina et al., 2017). In contrast, the Forchheimer number (Fo) corresponds to the ratio of the inertial and viscous term in the Forchheimer's law (Eq. 9; Degruyter et al., 2012; La Spina et al., 2017):

$$\mathrm{Fo} = \frac{\rho_{g0} k_1 U_o}{k_2 \mu_g} \quad (8)$$

$$\rho_{g0} = \frac{P_0}{RT} \quad (9)$$

where ρ_{g0} is the density of the gas phase and k_2 is the inertial permeability. The density of the gas phase is calculated using the Eq (9), where P_0 is the pressure in the conduit at a

certain depth and R is the specific gas constant. The inertial permeability is calculated using the Gonnermann et al. (2017) relationship between Darcian and Inertial permeabilities (Eq 10):

$$\log_{10}(k_2) = 1.353 \log_{10}(k_1) + 8.175 \qquad (10)$$

For small Fo, outgassing is controlled by the viscous permeability (Darcian). For larger Fo, the inertial permeability dominates (Degruyter et al., 2012; La Spina et al., 2017).

In order to obtain Fo and St values, we assumed that the temperature in the conduit is constant. We used a temperature of 1100 ˚C (1375 K), which represents the mean temperature for the Curacautín Ignimbrite pre-eruptive magma (Lohmar, 2008). Gas viscosity and velocity throughout the conduit are assumed constant as well, while conduit radius and reference depth are variable between 25 and 100 m, and between 100 and 1000 m, respectively. Parameters used for Fo and St computations are summarized in Table 3.

CHAPTER THREE: RESULTS

Reconstruction and measurements of vesicle textures in 3D

We analyzed 40 VOIs from 10 representative pyroclasts, 4 VOIs per sample. The reconstructed volumes obtained using synchrotron X-ray microtomography allow us to visualize and quantify the vesicle network of Llaima pyroclasts in 3D (Fig. 6). All samples show high vesicle interconnectivity and no signs of preferential vesicle elongation. There are two main populations of vesicles: (1) a contorted connected vesicle network produced by coalescence of smaller vesicles (>99% of porosity network, yellow color in Fig. 6A, and (2) a population of very small and completely isolated vesicles (<1% of porosity network; Fig. 6B). Isolated vesicles present multiple shapes with no evidence of high sphericity or preferential elongation.

Quantitative textural parameters as 2D and 3D vesicularities, bubble number densities (BND) and specific surface area are summarized in Table 1. Individual 3D measurements of vesicularities are shown in Fig. 7A; the 2D ranges are represented by the error bars. Average 3D vesicularities, correlated stratigraphically in Fig. 8A, and BND are presented in Table 1. The BND results correspond to less than 1% of the total vesicle phase (Fig. 6B). No correlation between BND and vesicularity is observed.

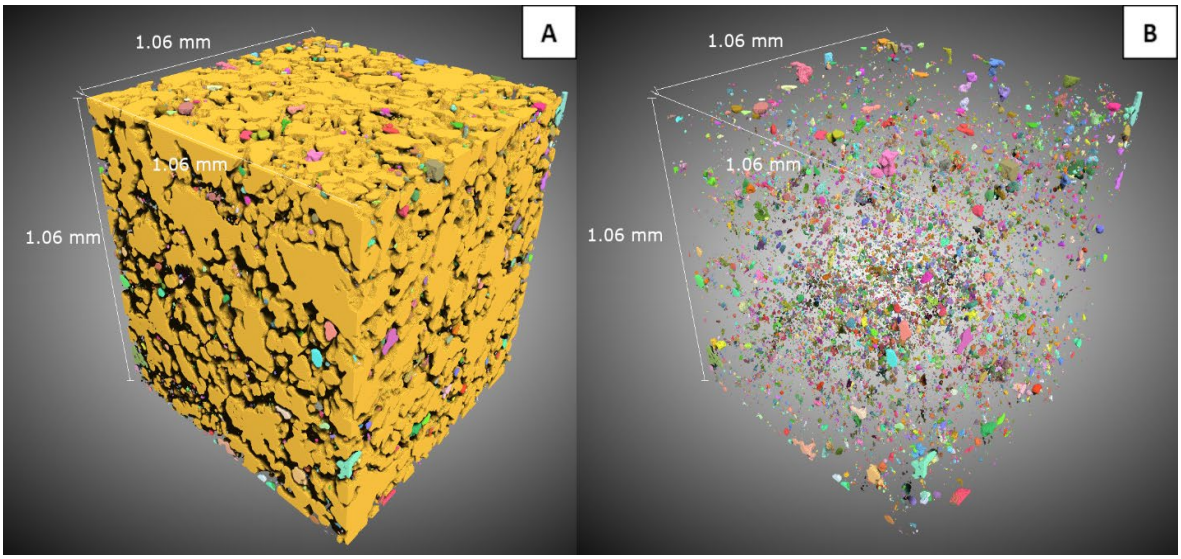

Figure 6 (A) 3D visualization of L4 vesicle network and isolated vesicles. Every color represents 1 single vesicle, where the yellow color represents the main convoluted connected vesicle network. All voids correspond to the solid phase. (B) 3D visualization of L4 isolated vesicles. Every color represents one single vesicle.

Table 1 Summary of X-ray microtomography results of vesicle textural analysis. Microlite number densities and density values extracted from Marshall et al. (in prep).

Sample ID(Unit)	2D porosity range (vol%)[a]	3D porosity (vol%)[b]	BND × 10^3 (mm^{-3})[c]	Specific surface area (mm^{-1}) S[d]	Tortuosity factor τ* [e]	Nv x 10^6 (mm^{-3})[f]	Density (kg m^{-3})[g]
L5(1)	45 - 68	57.02 (3.96)	7.96 (3.75)	81.69 (3.37)	2.72 (0.55)		
L1(1)	56 - 77	68.21 (3.14)	13.93 (5.12)	61.15 (5.84)	1.89 (0.24)	9.72	1320 (280)
L2(1)	41 - 63	53.00 (1.99)	4.13 (2.53)	68.99 (2.66)	3.99 (0.48)		1350 (300)
L3(1)	42 - 73	54.53 (4.74)	5.89 (2.25)	99.13 (15.83)	2.81 (0.64)	9.55	1210 (230)
L4(1)	45 - 59	51.83 (1.86)	8.83 (8.43)	92.15 (5.13)	3.74 (0.52)	13.3	1310 (280)
L12(1)	44 - 63	51.97 (4.77)	13.00 (8.02)	128.17 (27.46)	4.57 (1.36)		
L6(1)	47 - 65	56.28 (1.87)	7.88 (4.43)	74.68 (4.44)	3.09 (0.22)	8.21	1260 (270)
L8(2)	39 - 56	47.44 (1.68)	1.09 (0.42)	86.27 (3.61)	4.03 (0.39)	7.95	1320 (320)
L10(3)	39 - 55	48.11 (2.59)	23.06 (12.43)	111.86 (9.13)	3.75 (0.28)	16.6	1390 (370)
L18(4)	42 - 59	51.07 (4.23)	2.18 (1.51)	83.38 (8.74)	4.40 (0.82)	18.4	1410 (310)

[a]Minimum and maximum values of 2D porosity considering 4 VOIs per sample. [b]Average porosity values. Numbers in parenthesis indicate ±1σ, (n=4). [c]Average bubble number densities. Numbers in parenthesis indicate ±1σ, (n=4). [d]Average specific surface area, surface area per volume. Numbers in parenthesis indicate ±1σ, (n=4). [e]Average tortuosity factor values considering the 3 axis of interest. Numbers in parenthesis indicate ±1σ, (n=12). [f]Nv corresponds to plagioclase microlite number densities. (Marshal et al., in prep). [g]Sample density (Marshal et al., in prep). Numbers in parenthesis indicate the error.

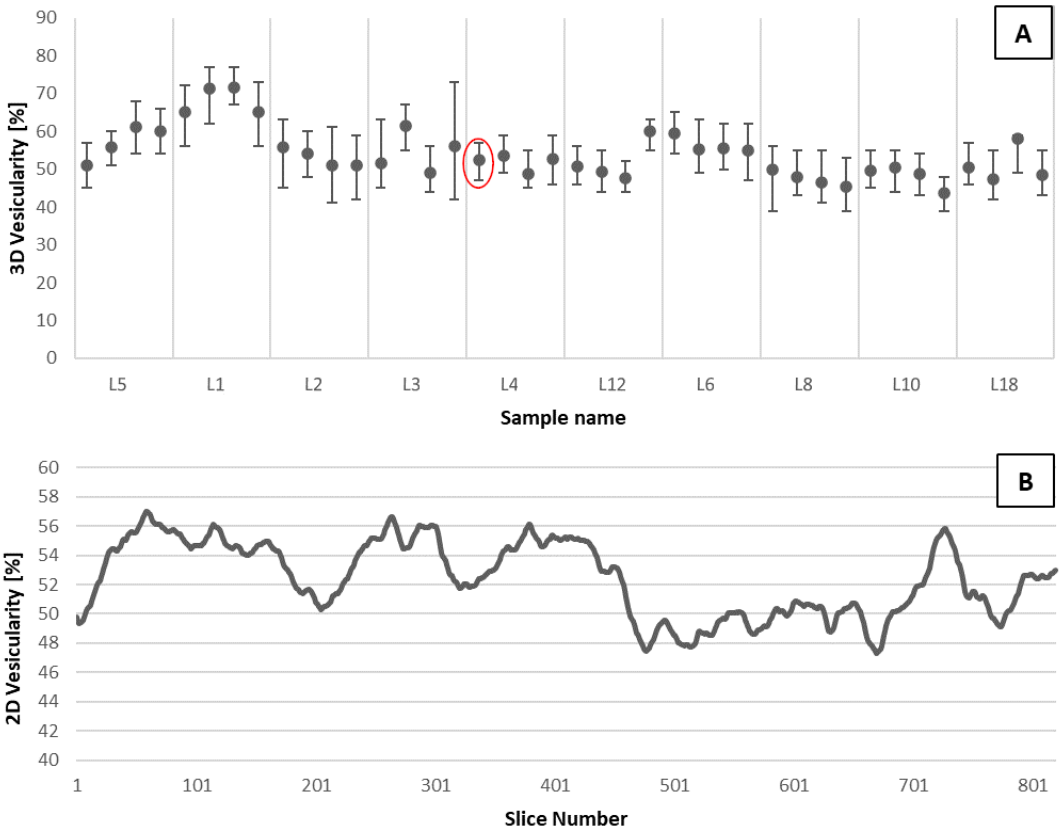

Figure 7 (A) 3D vesicularities measurements of the 4 VOIs per sample. Error bars correspond to 2D vesicularity ranges. (B) 2D vesicularity variability of one L4 sample marked in red. Maximum and minimum values represented in (A) as error bars.

Average specific surface area calculations, defined as the ratio between the surface area and the volume (Maroof et al., 2020), are also presented in Table 1. These values were calculated for the contorted connected phase that represents the 99% of the vesicle phase (Fig. 6A, yellow interconnected vesicle). No correlation with vesicularity or BND is observed.

Tortuosity factor

Tortuosity factors were calculated using the MATLAB application TauFactor, which quantifies the apparent decrease in diffusive transport resulting from convolutions of the flow paths through porous media (Cooper et al., 2016). We compute tortuosities

factors in three orthogonal directions following the axis of our cubic VOIs. Results are presented in Table 1 and correlated stratigraphically in Fig. 8B. We observe low directional variability, implying that there is no preferential path direction for the gas flux. We also observe an inverse relationship between vesicularity and tortuosity, and a strong direct correlation with specific surface area (Appendix A.1).

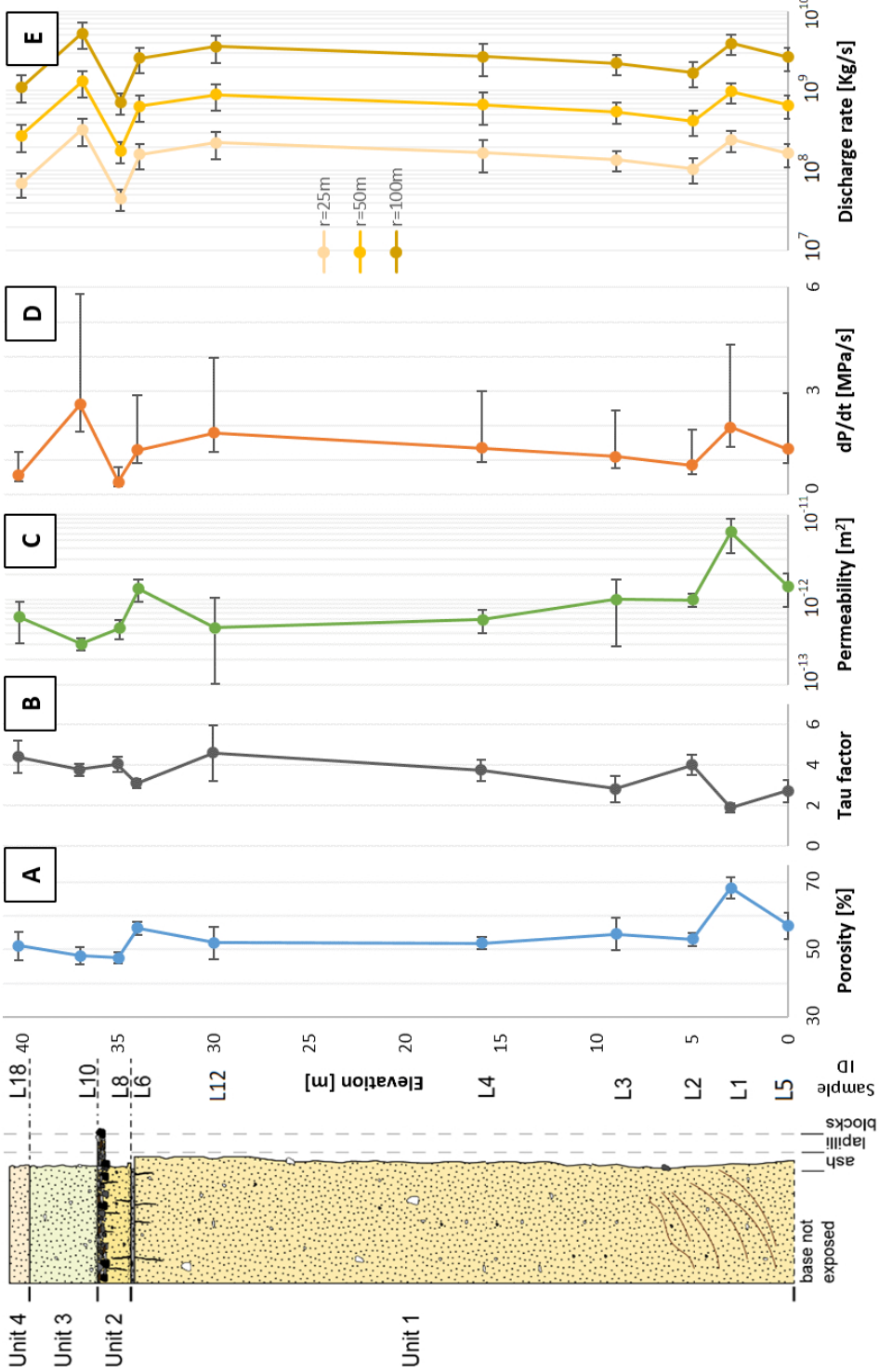

Figure 8 **Results summary related with their locations in the stratigraphic column. (A) Porosity (B) Tau factor (C) Darcian Permeability (D) Decompression Rates (E) Discharge rates for radii of 25, 50, and 100 m.**

Table 2 Summary of results for Darcian and Inertial permeabilities, Decompression rates, Discharge rates and Fragmentation threshold.

Sample ID(Unit)	Darcian Permeability $\times 10^{-12}$ (m^2) k_1[a]	Inertial Permeability $\times 10^{-8}$ (m) k_2[b]	Decompression rate (MPa s-1)[c]	Discharge rate x 10^8 (Kg s^{-1})			ΔPfr (MPa)[g]
				r_{25}[d]	r_{50}[e]	r_{100}[f]	
L5(1)	1.43 (0.61)	1.48 (0.81)	1.32 (0.39)(1.62)	1.65 (0.54)	6.59 (2.15)	26.4 (8.60)	4.32 (0.05)
L1(1)	6.27 (2.7)	10.5 (5.8)	1.95 (0.58)(2.40)	2.44 (0.71)	9.77 (2.83)	39.1 (11.3)	5.14 (0.21)
L2(1)	0.99 (0.18)	0.87 (0.19)	0.84 (0.25)(1.03)	1.05 (0.37)	4.21 (1.48)	16.8 (5.92)	4.39 (0.04)
L3(1)	1.00 (0.71)	1.07 (0.92)	1.10 (0.33)(1.35)	1.37 (0.40)	5.49 (1.62)	22.0 (6.47)	4.17 (0.09)
L4(1)	0.58 (0.18)	0.41 (0.16)	1.34 (0.40)(1.65)	1.68 (0.73)	6.72 (2.91)	26.9 (11.2)	4.11 (0.03)
L12(1)	0.47 (0.58)	0.38 (0.56)	1.78 (0.53)(2.19)	2.23 (0.83)	8.91 (3.32)	35.6 (13.3)	3.81 (0.10)
L6(1)	1.35 (0.39)	1.31 (0.52)	1.28 (0.38)(1.58)	1.61 (0.57)	6.44 (2.29)	25.8 (9.15)	4.36 (0.06)
L8(2)	0.46 (0.12)	0.27 (0.1)	0.36 (0.11)(0.44)	0.47 (0.13)	1.78 (0.56)	7.13 (2.10)	4.35 (0.04)
L10(3)	0.30 (0.05)	0.17 (0.03)	2.60 (0.78)(3.21)	3.20 (1.20)	13.1 (4.79)	52.2 (19.2)	4.08 (0.11)
L18(4)	0.62 (0.31)	0.57 (0.41)	0.55 (0.16)(0.68)	0.68 (0.25)	2.75 (0.96)	11.0 (3.94)	4.19 (0.06)

[a]Average Darcian permeability values considering the 3 axis of interest using Eq. 4 and c=8 (Bernabe et al., 2010; Farquharson et al., 2015). Numbers in parenthesis indicate ±1σ, (n=12). [b]Average Inertial permeability values calculated using Eq. 11 (Gonnermann et al., 2017). Numbers in parenthesis indicate ±1σ. (n=12). [c]Average decompression rates values using Eq. 5 (Toramaru, 2006; Shea, 2017). First and second number in parenthesis indicate the minimum and maximum value respectively, (n=4). [d]Average discharge rate for a 25 meters conduit radius using Eq. 6. Numbers in parenthesis indicate ±1σ, (n=4). [e]Average discharge rate for a 50 meters conduit radius using Eq. 6. Numbers in parenthesis indicate ±1σ, (n=4). [f]Average discharge rate for a 100 meters conduit radius using Eq. 6. Numbers in parenthesis indicate ±1σ, (n=4). [g]Fragmentation threshold (Mueller et al., 2008).

Permeability calculations

Darcian Permeabilities were calculated using Eq. (4) and assuming a pore-controlled medium (c = 8; Bernabe et al., 2010; Farquharson et al., 2015). Similar to the tortuosity factor calculations, we computed permeability values in three orthogonal directions following the axis of our cubic VOIs. Computations of average Darcian permeability are presented in Table 2 and correlated stratigraphically in Figure 8C. These results have an inverse correlation with tortuosity, a direct correlation with vesicularity, and a strong inverse correlation with the specific surface area. We calculated inertial permeabilities using the Darcian permeability results and the Eq. (11) (Gonnermann et al., 2017). Average values of inertial permeabilities are also presented in Table 2, and present similar correlations to Darcian permeabilities.

Decompression and discharge rates

Due to the large amount of microlites and the absence of glass in our samples (Fig. 2), we propose a heterogeneous nucleation regime for the formation of the small isolated vesicles (Fig. 6B). Therefore, we calculated decompression rates using the Eq. (5) proposed by Toramaru (2006) for basaltic magmas under heterogeneous nucleation (Shea, 2017). Decompression rates for all samples range from 0.36 to 2.60 MPa s^{-1} (Table 2; Fig. 8D). Figure 9, which compares our results with other basaltic eruptions (Toramaru, 2006; Shea, 2017), shows that the estimated decompression rates for the Curacautín magma are close to decompression rates calculated for Tarawera 1886AD and Etna 122BC. Finally, in order to calculate and contrast discharge rates with other basaltic eruptions, we use Eq. (6) for three different conduit radius (Table 2 and Fig. 8E).

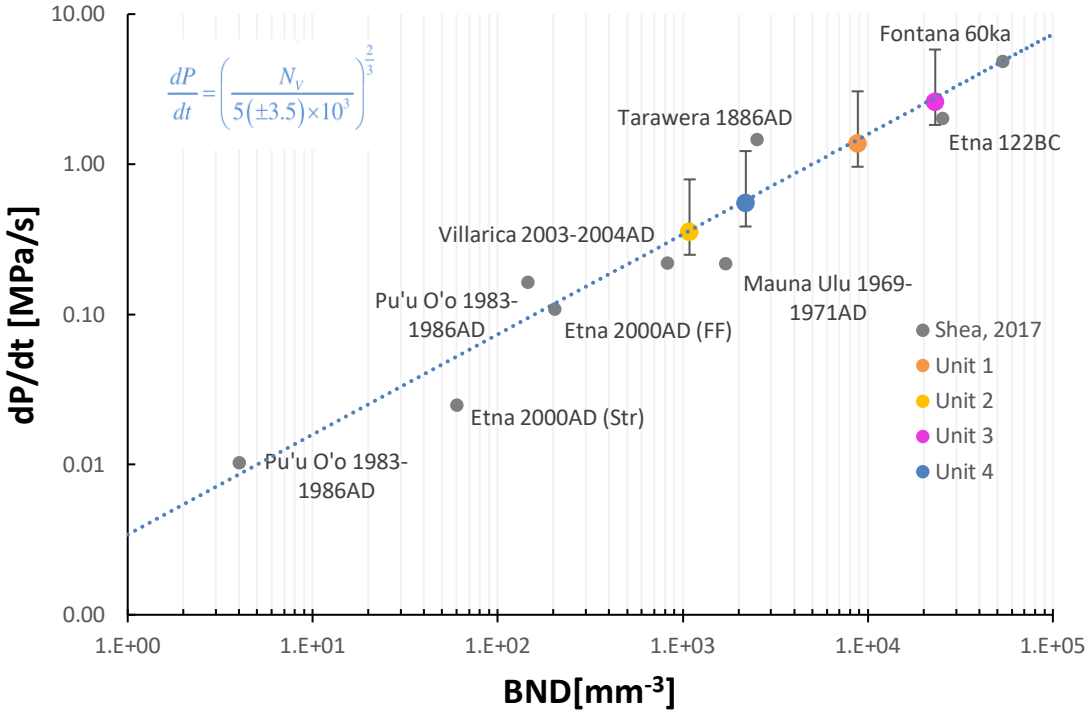

Figure 9 Decompression rates (MPa/s) vs BND (mm^{-3}) for Units 1-4 using Eq. 6 (Toramaru, 2006; Shea, 2017). The blue line corresponds to the equation shown in the top left corner. Historic basaltic eruptions extracted from Shea, 2017.

Forchheimer and Stokes numbers

We calculated Fo and St number for Unit 1 following equations 7, 8, 9, and 10 using the reference parameters in Table 3 (Degruyter et al., 2012; La Spina et al., 2017). The (St, Fo) results for Unit 1 overlap with the (St, Fo) values for the 1980 Mount St. Helens (MSH) Plinian eruption reported by Degruyter et al. (2012) (Fig. 10). Both areas are in the low St and high Fo regions, indicating that the magma and gas were coupled, ascending at the same velocity, and the outgassing was turbulent (Degruyter et al., 2012). Higher permeabilities resulted in higher and lower values of St and Fo, respectively, increasing the outgassing efficiency but not enough to decouple the gas phase from the magma. Conversely, lower permeabilities resulted in lower and higher values of St and Fo, respectively, enhancing the coupling between magma and the gas phase. Figure 10 shows how increasing certain parameters influence the St and Fo numbers.

Table 3 Reference parameters and results for calculation of Stokes and Forchheimer numbers.

Parameter	Symbol	Value(s)	Unit
Decompression rate[a]	dP/dt	1.37	MPa s^{-1}
Magmastatic gradient[b]	dP/dz	0.0265	MPa m^{-1}
Darcian permeability[c]	k_1	9.5×10^{-14} - 9.37×10^{-12}	m^2
Inertial permeability[d]	k_2	3.6×10^{-10} - 1.8×10^{-7}	m
Bulk magma density[e]	ρ_m	1290	kg m^{-3}
Gas viscosity[f]	μ_g	0.000015	Pa s
Mean velocity[g]	U_0	51.698	m s^{-1}
Reference temperature[h]	T	1375	K
Specific gas constant[i]	R	461.4	J kg^{-1} K^{-1}
Conduit radius	r	25 - 100	m
Reference depth	z	100 - 1000	m
Reference gas preassure	P_0	4.177 - 41.770	Pa
Forcheimer number	Fo	7.52×10^{2} - 3.8×10^{4}	-
Stokes number	St	3.68×10^{-6} - 1.67×10^{-3}	-

[a]Average value for Unit 1. [b]From Cas and Simmons (2018). [c]Range of Darcian permeability results for Unit 1 using Eq. 4. [d]Inertial Permeability ranges using Eq.10 (Gonnermann et al., 2017). [e]Average density for Unit 1 from Marshall et al. (in prep). [f,i]From Degruyter et al. (2012); La Spina et al. (2017). [g]Ratio between the mean decompression rate and the magmastatic gradient. [h]Mean temperature for the Curacautin Ignimbrite pre-eruptive magma (Lohmar, 2008).

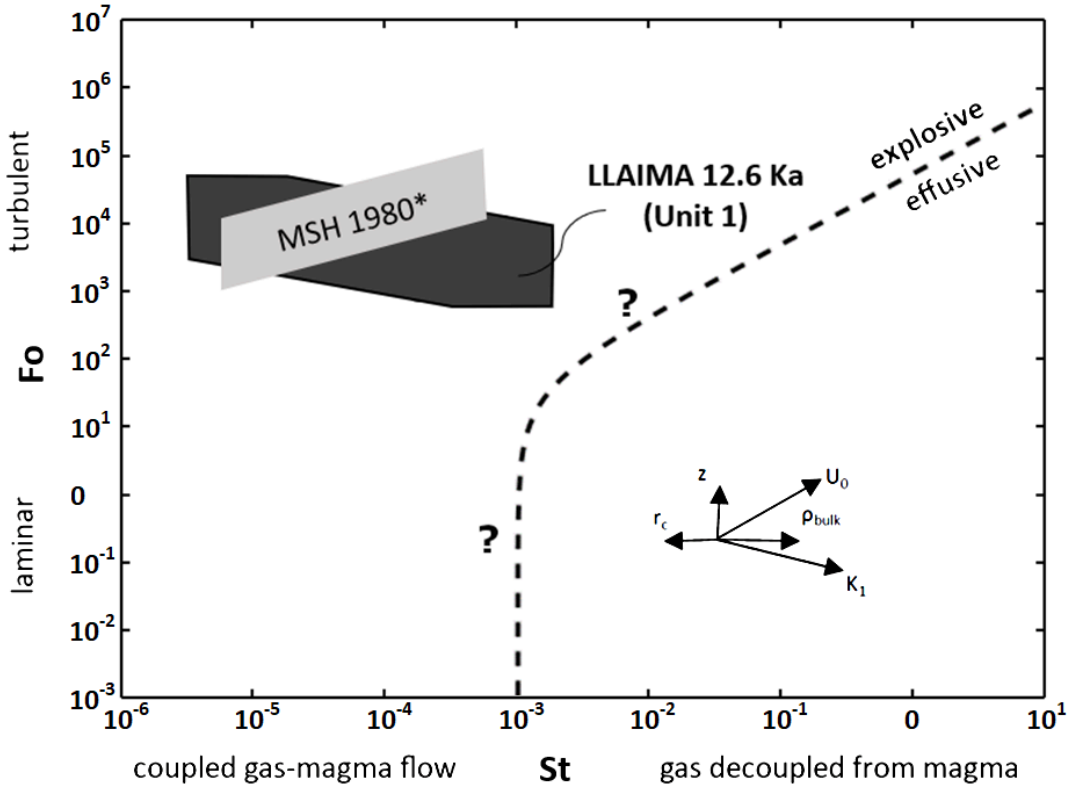

Figure 10 Stokes vs Forchheimer number plot. The dark grey region represents the (Fo, St) results for Unit 1 using the parameters shown in Table 1. The light grey area corresponds to the (Fo, St) values for the 1980 MSH Plinian eruption (Degruyter et al., 2012). The dash line represents a hypothetical boundary between effusive (below) and explosive (above) behavior for Llaima conduit (not computed because the crystallization kinetics and rheology are not well enough constrained). The arrows indicate how the results would change by increasing different parameters.

CHAPTER FOUR: DISCUSSION

The 3D reconstructions allow us to investigate the pyroclast textures in detail and extract valuable information, including vesicularity, surface areas, interconnectivity, and number of vesicles, all of which are more challenging to interpret in 2D slices. For example, we observe an average variation of ~13% for the 2D vesicularities considering all our VOIs (Fig. 7). That variation decreases to less than ~3% if we compare the 3D vesicularity between the four VOIs per sample (Table 1). This increment of accuracy suggests that the VOI selected for this research is sufficient to account for the major textural variabilities of our samples. In addition, we observe a vesicle network with more than 99% interconnectivity in all our samples, something that would be impossible to conclude with 2D section analyses. This argument also applies to BND calculations, where it is harder to discern if a vesicle is connected or not, especially under the presence of a convoluted vesicle network that looks more disconnected in 2D (Fig. 2; Fig. 6).

BND results suggest that the magma rose at fast decompression rates, similar to other basaltic explosive eruptions reported in the literature (Shea, 2017). Specifically, Unit 1 shows an average decompression rate of 1.4 MPa s^{-1} (Eq. 5), similar to the 1.5 and 2.0 MPa s^{-1} reported for Tarawera 1886AC and Etna 122BC, respectively (Figure 9; Shea, 2017). Although the lack of more samples for Unit 2, 3 and 4 add additional uncertainty to the results, their decompression rates show a similarly rapid ascent behavior. We estimate average discharge rates between 1.6×10^{8} and 2.2×10^{9} kg s^{-1} (Fig. 8E; Eq. 6), close

to the 1.4×10^8 kg s^{-1} and 5-8.5×10^8 kg s^{-1} reported for Fontana Lapilli Masaya 60ka and Etna 122BC, respectively (Shea, 2017).

The presence of two populations of vesicles implies that there were at least two events of bubble nucleation and growth in the magmatic system. We assume that the first vesiculation event occurred deeper in the conduit. Decompression expansion likely caused bubble growth and some degree of coalescence. Such vesiculation would have enhanced the buoyancy of the bulk magma, driving magma acceleration (Cassidy et al., 2018).

The formation of the second population of vesicles (~1% of isolated vesicles; Fig 6B) might be the result of a syn-eruptive or late stage crystallization of microlites induced by rapid ascent rates (La Spina et al., 2016). Decompression experiments show that rapid ascent rates lead to high degrees of disequilibrium, promoting rapid nucleation of plagioclase microlites at shallow depths (Brugger and Hammer, 2010; Befus and Andrews, 2018). Our samples are rich in microlites, with microlite number densities between of 7.95-18.4×10^8 plagioclase microlites per mm^3 (Marshall et al., in prep; Table 1), evidencing high degrees of disequilibrium crystallization. We infer that microlite nucleation shifted the solubility conditions of the remaining melt (Hajimirza et al., 2021), causing a second, late-stage exsolution event that formed the smaller and isolated vesicles. Simultaneously, rapid crystallization of microlites would have restricted bubble expansion of the first population of vesicles forcing them to grow toward each other resulting in a tortuous vesicle network structure (99% interconnectivity) controlled by the geometry of plagioclase microlites (Fig. 2; Arzilli et al., 2019; deGraffenried et al., 2019). This contorted vesicle network shape and abundance of microlites between vesicles would limit the diffusion of the remaining dissolved volatiles to existing bubbles and provide sites for

heterogeneous nucleation, leading the nucleation of the disconnected group of vesicles (Hajimirza et al., 2021).

Fo and St calculations for Unit 1 (Eq. 8 and 9) suggest that the gas phase was coupled with the magma during ascent, similar to the Plinian phase of the 1980 MSH eruption (Degruyter et al., 2012). We propose that despite the well-connected network of vesicles promoted by crystallization (e.g., Lindoo et al., 2017), the high viscosity of the magma hindered the growth of pathways for gas transport through the convoluted vesicle network leading to the coupling of the gas with the magma during ascent. The restricted growth and coalescence, in addition to the late bubble nucleation event, may have generated enough overpressure to the system to lead to brittle fragmentation of the magma (Gonnermann and Manga, 2007). Given the evidence for rapid ascent rates, shear-induced fragmentation may also have played a role.

As a preliminary validation, our permeability calculations indicate that our samples are similar to those of other explosive eruptions (Fig. 11). Additionally, our results fall within the wide empirical bounds provided by Mueller et al. (2005) for explosive volcanic rocks and are consistent with collected data from pyroclasts from explosive eruptions (Degruyter et al., 2012; Wright et al., 2009). Our values are similar to those measured on samples generated experimentally in crystallizing and vesiculating basaltic andesites (Lindoo et al., 2017). In order to assign a degree of accuracy to our work and given the small size of pyroclast available for this research, we propose further experimental validation of our methodology using other volcanic products, sufficiently large in size for traditional permeameters, or Lattice-Boltzmann simulations (Degruyter et al., 2010).

Following the methods of Mueller et al. (2008), we calculate the minimum bubble overpressure needed to lead fragmentation (ΔP_{fr})

$$\Delta P_{\mathrm{fr}} = \frac{a\sqrt{k_1} + \sigma_m}{\phi} \qquad (11)$$

where a and σ_m are constants equal to 8.21×10^5 MPa m^{-1}, and 1.54 MPa, respectively. Our results show that a bubble overpressure greater than 5.2 MPa could have been sufficient to fragment the Curacautín magma (Fig. 12; Table 2).

Lastly, low variations in the stratigraphic sequence (Fig. 8) support the assertion of Marshall et al (in prep.) that the Curacautín Ignimbrite is the result of one eruptive event with perhaps several discrete explosive pulses, resulting in the four flow units.

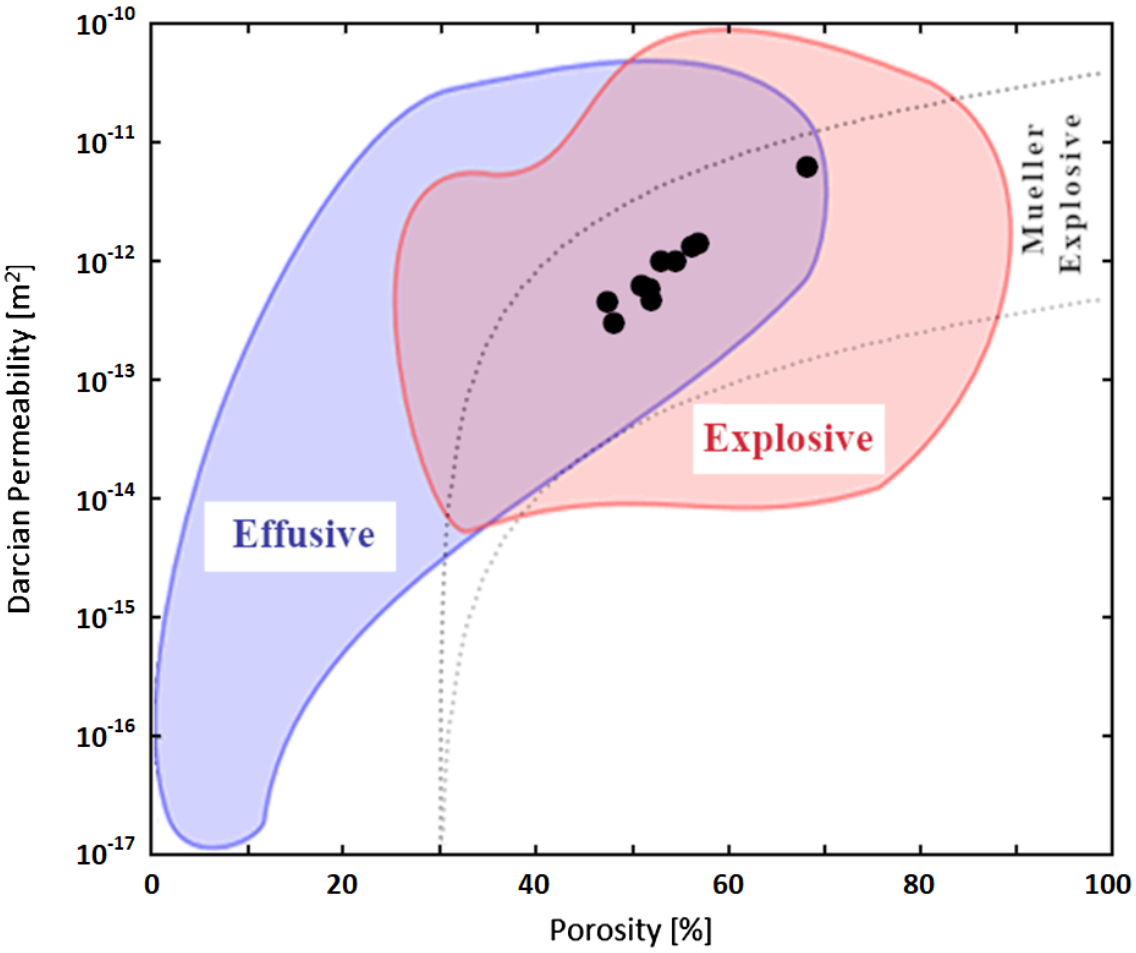

Figure 11 Porosity vs Darcian permeability results. Black dots correspond to the values calculated for the 12.6 ka Curacautín Ignimbrite (Eq. 4). The blue region represents data collection of pyroclasts for effusive eruptions, the red region represents data collection of pyroclasts for explosive eruptions (Degruyter et al., 2012; Wright et al., 2009). The area between the dash lines correspond to the Mueller et al. (2005) model for explosive eruptions.

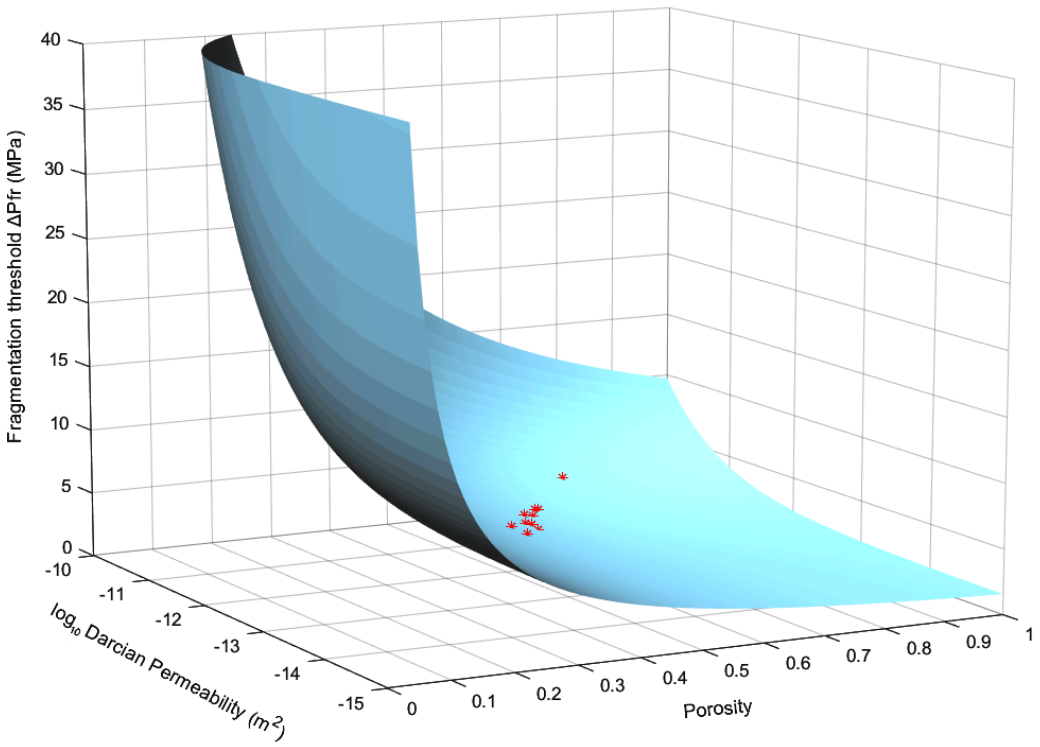

Figure 12 The 3D curve represents the minimum overpressure required to achieve fragmentation at given sample porosity and permeability (Mueller et al., 2008). Red stars represent our results for permeability and porosity.

CHAPTER FIVE: CONCLUSIONS

We focus on the 12.6 ka explosive mafic eruption at Llaima Volcano, Chile, that resulted in an extensive ignimbrite. The objective of this study was to use 3D X-ray microtomography reconstructions of pyroclasts to measure porosities, bubble number density, vesicle interconnectivity, and geometrical properties of the porous media. We use these textures to constrain vesicle tortuosity, permeabilities, decompression rates, the degree of coupling between the gas phase and the magma, and the evolution of vesiculation during ascent. The analytical calculations provide an approach for quantifying the permeability and tortuosity of pyroclasts vesicle networks in samples too small to use laboratory techniques (e.g., permeameter).

The 3D geometrical parameters extracted from X-ray microtomography analyses provides high degrees of accuracy than using 2D approaches, allowing us to accurately characterize the texture of our pyroclasts. Even though the relationship between tau factor and tortuosity is not well constrained yet, tau factor produced a reasonable approximation of tortuosity for the complex and convoluted vesicle networks of our pyroclasts without requiring high computational power. In order to validate the methodology used in this research, we propose further experimental research using bigger pyroclast products to compare X-ray microtomography permeabilities with permeameter calculations.

Our 3D vesicle texture results evidence rapid ascent rates that induced disequilibrium crystallization of microlites during ascent. The increase in microlite content

shifted the solubility of the remaining magma causing a second vesiculation, completely disconnected from the existing vesicle network. Simultaneously, microlite crystallization confined bubbles during expansion, enhancing bubble coalescence (connectivity). This crystallization event forced bubbles to grow toward each other, resulting in the convoluted interconnected vesicle network. At this stage, volatile phase was coupled with the magma inhibiting outgassing and promoting an increase in bubble overpressure. Our permeability and vesicularity results suggest that a minimum bubble overpressure of 5.2 MPa was required to induce fragmentation of the magma.

The conditions that led to explosive mafic volcanism at Llaima Volcano are similar to other basaltic explosive eruptions (Tarawera 1886AC, Etna 122BC and Fontana Lapilli Masaya 60ka). Our results provide further evidence that mafic explosive volcanism at Llaima volcano, as well as other mafic centers, is driven by rapid magma ascent. Rapid ascent induces disequilibrium crystallization conditions and rapid crystallization of microlites. Crystallization increased viscosity of the magma, inhibiting gas escape. We suggest that future work should focus on the evaluation of rheology evolution due to nucleation and growth of microlites during ascent, the mechanism behind the initiation and evolution of the vesicle network, and the conditions that lead to coupling of the gas and magma, promoting explosive behavior.

REFERENCES

Arzilli, F., La Spina, G., Burton, M., Polacci, M., Le Gall, N., Hartley, M., Di Genova, D., Cai, B., Vo, N., Bamber, E., Nonni, S., Atwood, R., Llewellin, E., Brooker, R., Mader, H., & Lee, P. (2019). Magma fragmentation in highly explosive basaltic eruptions induced by rapid crystallisation. Nature Geoscience, 12, 1023–1028. https://doi.org/10.1038/s41561-019-0468-6

Backeberg, N. R., Iacoviello, F., Rittner, M., Mitchell, T. M., Jones, A. P., Day, R., … Striolo, A. (2017). Quantifying the anisotropy and tortuosity of permeable pathways in clay-rich mudstones using models based on X-ray tomography. Scientific Reports, 7(1), 1–12. https://doi.org/10.1038/s41598-017-14810-1

Baker, D. R., Mancini, L., Polacci, M., Higgins, M. D., Gualda, G. A. R., Hill, R. J., & Rivers, M. L. (2012). An introduction to the application of X-ray microtomography to the three-dimensional study of igneous rocks. Lithos, 148, 262–276. https://doi.org/10.1016/j.lithos.2012.06.008

Bamber, E. C., Arzilli, F., Polacci, M., Hartley, M. E., Fellowes, J., Di Genova, D., … Burton, M. R. (2020). Pre- and syn-eruptive conditions of a basaltic Plinian eruption at Masaya Volcano, Nicaragua: The Masaya Triple Layer (2.1 ka). *Journal of Volcanology and Geothermal Research*, *392*, 106761. https://doi.org/10.1016/j.jvolgeores.2019.106761

Befus, K. S., & Andrews, B. J. (2018). Crystal nucleation and growth produced by continuous decompression of Pinatubo magma. Contributions to Mineralogy and Petrology, 173(11). https://doi.org/10.1007/s00410-018-1519-5

Berg, C. F. (2014). Permeability Description by Characteristic Length, Tortuosity, Constriction and Porosity. Transport in Porous Media, 103(3), 381–400. https://doi.org/10.1007/s11242-014-0307-6

Bernabé, Y., Li, M., Maineult, A. (2010). Permeability and pore connectivity: a new model based on network simulations. J. Geophys. Res. 155, B10203. http://dx.doi.org/10.1023/2010JB007444

Bernard, M. L., Zamora, M., Géraud, Y., & Boudon, G. (2007). Transport properties of pyroclastic rocks from Montagne Pelée volcano (Martinique, Lesser Antilles). Journal of Geophysical Research: Solid Earth, 112(5), 1–16. https://doi.org/10.1029/2006JB004385

Brugger, C. R., & Hammer, J. E. (2010). Crystallization kinetics in continuous decompression experiments: Implications for interpreting natural magma ascent processes. Journal of Petrology, 51(9), 1941–1965. https://doi.org/10.1093/petrology/egq044

Cas, R. A. F., & Simmons, J. M. (2018). Why deep-water eruptions are so different from subaerial eruptions. Frontiers in Earth Science, 6(November), 1–21. https://doi.org/10.3389/feart.2018.00198

Cashman, K. V., & Scheu, B. (2015). Magmatic Fragmentation. In The Encyclopedia of Volcanoes (Second Edi). https://doi.org/10.1016/b978-0-12-385938-9.00025-0

Cassidy, M., Manga, M., Cashman, K., & Bachmann, O. (2018). Controls on explosive-effusive volcanic eruption styles. Nature Communications, 9(1). https://doi.org/10.1038/s41467-018-05293-3

Coltelli M, Del Carlo P, Vezzoli L (1998) Discovery of a Plinian basaltic eruption of Roman age at Etna volcano, Italy. Geology 26:1095–1098

Costantini L, Bonadonna C, Houghton BF, Wehrmann H (2009) New physical characterization of the Fontana Lapilli basaltic Plinian eruption, Nicaragua. Bull Volcanol 71:337–355. https://doi.org/10.1007/s00445-008-0227-9

Costantini L, Houghton BF, Bonadonna C (2010) Constraints on eruption dynamics of basaltic explosive activity derived from chemical and microtextural study: The example of the Fontana Lapilli Plinian eruption, Nicaragua. J Volcanol Geotherm Res 189:207–224. https://doi.org/j.jvolgeores.2009.11.008

Cooper, S. J., Bertei, A., Shearing, P. R., Kilner, J. A., & Brandon, N. P. (2016). TauFactor: An open-source application for calculating tortuosity factors from tomographic data. SoftwareX, 5, 203–210. https://doi.org/10.1016/j.softx.2016.09.002

deGraffenried, R. L., Larsen, J. F., Graham, N. A., & Cashman, K. V. (2019). The Influence of Phenocrysts on Degassing in Crystal-Bearing Magmas With Rhyolitic Groundmass Melts. *Geophysical Research Letters*, *46*(10), 5127–5136. https://doi.org/10.1029/2018GL081822

Degruyter, W., Burgisser, A., Bachmann, O., & Malaspinas, O. (2010). Synchrotron X-ray microtomography and lattice Boltzmann simulations of gas flow through volcanic pumices. Geosphere, 6(5), 470–481. https://doi.org/10.1130/GES00555.1

Degruyter, W., Bachmann, O., Burgisser, A., & Manga, M. (2012). The effects of outgassing on the transition between effusive and explosive silicic eruptions. Earth and Planetary Science Letters, 349–350, 161–170. https://doi.org/10.1016/j.epsl.2012.06.056

Farquharson, J., Heap, M. J., Varley, N. R., Baud, P., & Reuschlé, T. (2015). Permeability and porosity relationships of edifice-forming andesites: A combined field and laboratory study. Journal of Volcanology and Geothermal Research, 297, 52–68. https://doi.org/10.1016/j.jvolgeores.2015.03.016

Giachetti, T., Burgisser, A., Arbaret, L., Druitt, T. H., & Kelfoun, K. (2011). Quantitative textural analysis of Vulcanian pyroclasts (Montserrat) using multi-scale X-ray computed microtomography: Comparison with results from 2D image analysis. *Bulletin of Volcanology*, *73*(9), 1295–1309. https://doi.org/10.1007/s00445-011-0472-1

Gonnermann, H. M., & Manga, M. (2007). The fluid mechanics inside a volcano. Annual Review of Fluid Mechanics, 39, 321–356. https://doi.org/10.1146/annurev.fluid.39.050905.110207

Gonnermann, H. M., Giachetti, T., Fliedner, C., Nguyen, C. T., Carey, R. J., Houghton, B. F., & Crozier, J. A. (2017). Journal of Geophysical Research : Solid Earth. Permeability During Magma Expansion and Compaction. 1–24.

Hajimirza, S., Gonnermann, H. M., & Gardner, J. E. (2021). Reconciling bubble nucleation in explosive eruptions with geospeedometers. *Nature Communications, 12(1), 1-8.*

Houghton BF, Wilson CJN, Del Carlo P, Coltelli M, Sable JE, Carey R (2004) The influence of conduit processes on changes in styles of basaltic Plinian eruptions: Tarawera 1886 and Etna 122 BC. J Volcanol Geotherm Res 137:1–14. https://doi.org/j.jvolgeores.2004.05.009

Ketcham, R. A., & Carlson, W. D. (2001). Acquisition, optimization and interpretation of x-ray computed tomographic imagery: Applications to the geosciences. Computers and Geosciences, 27(4), 381–400. https://doi.org/10.1016/S0098-3004(00)00116-3

Ketcham, R. A. (2005). Computational methods for quantitative analysis of three-dimensional features in geological specimens. Geosphere, 1(1), 32–41. https://doi.org/10.1130/GES00001.1

Klug, C., Cashman, K. Permeability development in vesiculating magmas: implications for fragmentation. *Bull Volcanol* 58, 87–100 (1996). https://doi-org.libproxy.boisestate.edu/10.1007/s004450050128

La Spina, G., Burton, M., De'Michieli Vitturi, M., & Arzilli, F. (2016). Role of syn-eruptive plagioclase disequilibrium crystallization in basaltic magma ascent dynamics. Nature Communications, 7(November 2017). https://doi.org/10.1038/ncomms13402

La Spina, G., Polacci, M., Burton, M., & de' Michieli Vitturi, M. (2017). Numerical investigation of permeability models for low viscosity magmas: Application to the 2007 Stromboli effusive eruption. Earth and Planetary Science Letters, 473, 279–290. https://doi.org/10.1016/j.epsl.2017.06.013

La Spina, G., Arzilli, F., Llewellin, E. W., Burton, M. R., Clarke, A. B., de' Michieli Vitturi, M., … Mader, H. M. (2020). Explosivity of basaltic lava fountains is controlled by magma rheology, ascent rate and outgassing. Earth and Planetary Science Letters, 553, 116658. https://doi.org/10.1016/j.epsl.2020.116658

Lindoo, A., Larsen, J. F., Cashman, K. V., & Oppenheimer, J. (2017). Crystal controls on permeability development and degassing in basaltic andesite magma. *Geology*, *45*(9), 831-834.

Lohmar, S. (2008). Petrologia de las ignimbritas Lican y Pucon (Volcan Villarrica) y Curacautín (Volcan Llaima) en los Andes del sur de Chile. Universidad de Chile.

Mangan, M., Sisson, T. (2000). Delayed, disequilibrium degassing in rhyolite magma: decompression experiments and implications for explosive volcanism. Earth and Planetary Science Letters 183, 441–455.

Mangan, M., Mastin, L., Sisson, T. (2004). Gas evolution in eruptive conduits: combining insights from high temperature and pressure decompression experiments with steady-state flow modelling. Journal of Volcanology and Geothermal Research 129, 23–36

Maroof, M. A., Mahboubi, A., & Noorzad, A. (2020). A new method to determine specific surface area and shape coefficient of a cohesionless granular medium. Advanced Powder Technology, 31(7), 3038–3049. https://doi.org/10.1016/j.apt.2020.05.028

Martel, C., & Iacono-marziano, G. (2015). Timescales of bubble coalescence , outgassing , and foam collapse in decompressed rhyolitic melts. *Earth and Planetary Science Letters*, *412*, 173–185. https://doi.org/10.1016/j.epsl.2014.12.010

Matyka, M., & Koza, Z. (2011). Tortuosity-porosity relation in porous media flow. (May 2014). https://doi.org/10.1103/PhysRevE.78.026306

Moitra, P., Gonnermann, H. M., Houghton, B. F., & Tiwary, C. S. (2018). Fragmentation and Plinian eruption of crystallizing basaltic magma. *Earth and Planetary Science Letters*, *500*, 97–104. https://doi.org/10.1016/j.epsl.2018.08.003

Mueller, S., Melnik, O., & Spieler, O. (2005). Permeability and degassing of dome lavas undergoing rapid decompression : An experimental determination. 526–538. https://doi.org/10.1007/s00445-004-0392-4

Mueller, S., Scheu, B., Spieler, O., & Dingwell, D. B. (2008). Permeability control on magma fragmentation. Geology, 36(5), 399–402. https://doi.org/10.1130/G24605A.1

Murch, A. P., & Cole, P. D. (2019). Using microlites to gain insights into ascent conditions of differing styles of volcanism at Soufrière Hills Volcano. Journal of Volcanology and Geothermal Research, 384, 221–231. https://doi.org/10.1016/j.jvolgeores.2019.07.022

Namiki, A., Patrick, M. R., Manga, M., & Houghton, B. F. (2021). Brittle fragmentation by rapid gas separation in a Hawaiian fountain. *Nature Geoscience*, 1-6.

Naranjo, J., & Moreno, M. (1991). Actividad explosiva postglacial en el volcan Llaima, Andes del Sur, 38° 45S. *Rev. Geol. Chile*, *18*(1), 69–80. https://doi.org/10.5027/andgeoV18n1-a06

Pandolfi, R. J. et al. (2018). Xi-cam: a versatile interface for data visualization and analysis. J. Synchrotron Radiation 25, 1261–1270.

Parfitt, E. A. (2004). A discussion of the mechanisms of explosive basaltic eruptions. Journal of Volcanology and Geothermal Research, 134(1–2), 77–107. https://doi.org/10.1016/j.jvolgeores.2004.01.002

Pérez W, Freundt A, Kutterolf S (2020) The basaltic plininan eruption of the ~6 ka San Antonio Tephra and formation of the Masaya caldera, Nicaragua. J Volcanol Geotherm Res 401:1–17. doi: 10.1016/j.jvolgeores.2020.106975

Polacci, M., Mancini, L., & Baker, D. R. (2010). The contribution of synchrotron X-ray computed microtomography to understanding volcanic processes. *Journal of Synchrotron Radiation*, *17*(2), 215–221. https://doi.org/10.1107/S0909049509048225

Polacci, M., Arzilli, F., La Spina, G., Le Gall, N., Cai, B., Hartley, M. E., … Burton, M. R. (2018). Crystallisation in basaltic magmas revealed via in situ 4D synchrotron X-ray microtomography. *Scientific Reports*, *8*(1), 1–13. https://doi.org/10.1038/s41598-018-26644-6

Sable, J. E., Houghton, B. F., Del Carlo, P., & Coltelli, M. (2006). Changing conditions of magma ascent and fragmentation during the Etna 122 BC basaltic Plinian eruption: Evidence from clast microtextures. *Journal of Volcanology and Geothermal Research*, *158*(3–4), 333–354. https://doi.org/10.1016/j.jvolgeores.2006.07.006

Shanti, N. O., Chan, V. W. L., Stock, S. R., De Carlo, F., Thornton, K., & Faber, K. T. (2014). X-ray micro-computed tomography and tortuosity calculations of percolating pore networks. Acta Materialia, 71, 126–135. https://doi.org/10.1016/j.actamat.2014.03.003

Shea, T. (2017). Bubble nucleation in magmas : A dominantly heterogeneous process ? Journal of Volcanology and Geothermal Research, 343, 155–170. https://doi.org/10.1016/j.jvolgeores.2017.06.025

Suman, R., & Ruth, D. (1993). Formation factor and tortuosity of homogeneous porous media. Transport in Porous Media, 12(2), 185–206. https://doi.org/10.1007/BF00616979

Tjaden, B., Cooper, S. J., Brett, D. J., Kramer, D. & Shearing, P. R. (2016). On the origin and application of the Bruggeman correlation for analysing transport phenomena in electrochemical systems. Current Opinion in Chemical Engineering 12, 44–51

Toramaru, A. (2006). BND (bubble number density) decompression rate meter for explosive volcanic eruptions. 154, 303–316. https://doi.org/10.1016/j.jvolgeores.2006.03.027

Vona, A., Romano, C., Dingwell, D. B., & Giordano, D. (2011). The rheology of crystal-bearing basaltic magmas from Stromboli and Etna. *Geochimica et Cosmochimica Acta*, *75*(11), 3214–3236. https://doi.org/10.1016/j.gca.2011.03.031

Yokoyama, T., & Takeuchi, S. (2009). Porosimetry of vesicular volcanic products by a water-expulsion method and the relationship of pore characteristics to permeability. Journal of Geophysical Research: Solid Earth, 114(2). https://doi.org/10.1029/2008JB005758

Yoshimura, S., Kuritani, T., Matsumoto, A., & Nakagawa, M. (2019). Fingerprint of silicic magma degassing visualised through chlorine microscopy. Scientific Reports, 9(1), 1–10. https://doi.org/10.1038/s41598-018-37374-0

Wei, W., Cai, J., Xiao, J., Meng, Q., Xiao, B., & Han, Q. (2018). Kozeny-Carman constant of porous media: Insights from fractal-capillary imbibition theory. Fuel, 234(June), 1373–1379. https://doi.org/10.1016/j.fuel.2018.08.012

Wright, H. M. N., Cashman, K. V., Gottesfeld, E. H., & Roberts, J. J. (2009). Pore structure of volcanic clasts: Measurements of permeability and electrical conductivity. Earth and Planetary Science Letters, 280(1–4), 93–104. https://doi.org/10.1016/j.epsl.2009.01.023

APPENDIX

Table A.1 Full compilation of X-ray microtomography results of vesicle textural analysis, tortuosity factors, Darcian permeabilities and inertial permeabilities.

ID	2D porosity (vol%)	3D porosity (vol%)	BND (mm^{-3})	S (mm^{-1})	Tortuosity factor			Darcian Permeability (m^2)			Inertial Permeability (m)		
					d1	d2	d3	d1	d2	d3	d1	d2	d3
L5	45 - 57	51.04	1.80E+03	84.58	3.46	3.44	3.70	6.72E-13	6.75E-13	6.28E-13	5.07E-09	5.11E-09	4.63E-09
	51 - 60	55.88	8.09E+03	85.27	2.75	2.59	2.84	1.09E-12	1.16E-12	1.05E-12	9.80E-09	1.06E-08	9.34E-09
	54 - 68	61.02	1.11E+04	77.17	2.53	2.11	2.21	1.89E-12	2.27E-12	2.16E-12	2.05E-08	2.63E-08	2.46E-08
	54 - 66	60.13	1.09E+04	79.75	2.55	2.15	2.26	1.68E-12	1.98E-12	1.89E-12	1.75E-08	2.19E-08	2.06E-08
L1	56 - 72	65.07	1.90E+04	66.99	2.00	2.09	2.20	3.83E-12	3.67E-12	3.50E-12	5.35E-08	5.05E-08	4.73E-08
	62 - 77	71.16	7.52E+03	55.50	1.57	1.56	1.59	9.31E-12	9.37E-12	9.20E-12	1.78E-07	1.79E-07	1.75E-07
	67 - 77	71.54	1.03E+04	55.13	1.75	1.78	1.83	8.61E-12	8.47E-12	8.25E-12	1.60E-07	1.56E-07	1.51E-07
	56 - 73	65.07	1.90E+04	66.99	2.00	2.09	2.20	3.83E-12	3.67E-12	3.50E-12	5.35E-08	5.05E-08	4.73E-08
L2	45 - 63	55.77	5.57E+03	70.42	3.64	3.22	3.46	1.20E-12	1.36E-12	1.27E-12	1.11E-08	1.31E-08	1.19E-08
	48 - 60	54.01	7.54E+03	72.61	4.05	3.58	3.96	9.22E-13	1.04E-12	9.44E-13	7.78E-09	9.22E-09	8.03E-09
	41 - 61	51.08	1.99E+03	67.00	4.16	3.93	4.06	8.93E-13	9.44E-13	9.14E-13	7.45E-09	8.04E-09	7.69E-09
	42 - 59	51.13	1.41E+03	65.95	4.97	4.42	4.44	7.73E-13	8.69E-13	8.65E-13	6.13E-09	7.19E-09	7.15E-09
L3	45 - 63	51.47	7.43E+03	109.11	3.17	3.64	3.09	4.51E-13	3.93E-13	4.64E-13	2.96E-09	2.46E-09	3.07E-09
	55 - 67	61.54	8.45E+03	79.05	2.46	2.45	2.15	1.90E-12	1.90E-12	2.17E-12	2.07E-08	2.08E-08	2.48E-08
	44 - 56	49.12	5.04E+03	119.15	3.97	3.42	2.91	2.63E-13	3.05E-13	3.58E-13	1.43E-09	1.75E-09	2.17E-09
	42 - 73	55.99	2.64E+03	89.21	2.28	2.18	2.06	1.21E-12	1.26E-12	1.34E-12	1.13E-08	1.19E-08	1.29E-08
L4	47 - 57	52.39	2.34E+04	90.65	3.96	4.13	4.22	5.53E-13	5.30E-13	5.19E-13	3.90E-09	3.68E-09	3.57E-09
	49 - 59	53.57	3.34E+03	84.82	3.22	3.24	3.38	8.31E-13	8.24E-13	7.90E-13	6.76E-09	6.68E-09	6.32E-09
	45 - 55	48.69	3.98E+03	98.82	3.97	4.43	4.51	3.72E-13	3.33E-13	3.27E-13	2.28E-09	1.97E-09	1.92E-09
	46 - 59	52.65	4.57E+03	94.32	3.07	3.41	3.31	6.67E-13	6.01E-13	6.20E-13	5.03E-09	4.36E-09	4.55E-09

ID	2D porosity (vol%)	3D porosity (vol%)	BND (mm^{-3})	S (mm^{-1})	Tortuosity factor			Darcian Permeability (m^2)			Inertial Permeability (m)		
					d1	d2	d3	d1	d2	d3	d1	d2	d3
L12	46 - 56	50.83	2.27E+04	131.69	4.89	4.88	5.47	1.93E-13	1.94E-13	1.73E-13	9.41E-10	9.46E-10	8.09E-10
	44 - 55	49.42	1.01E+04	131.57	4.90	5.77	6.63	1.78E-13	1.51E-13	1.31E-13	8.39E-10	6.74E-10	5.58E-10
	44 - 52	47.63	1.77E+04	163.23	4.26	5.13	5.32	1.19E-13	9.88E-14	9.53E-14	4.88E-10	3.79E-10	3.61E-10
	55 - 63	60.00	1.48E+03	86.19	2.37	2.62	2.62	1.53E-12	1.38E-12	1.39E-12	1.55E-08	1.35E-08	1.35E-08
L6	54 - 65	59.51	1.28E+04	68.61	2.94	2.81	2.88	1.91E-12	1.99E-12	1.94E-12	2.08E-08	2.21E-08	2.14E-08
	49 - 63	55.13	1.02E+03	72.26	2.96	2.90	2.87	1.36E-12	1.38E-12	1.40E-12	1.31E-08	1.35E-08	1.36E-08
	50 - 62	55.40	7.75E+03	78.94	3.26	3.19	3.37	1.05E-12	1.07E-12	1.01E-12	9.24E-09	9.52E-09	8.84E-09
	47 - 62	55.06	9.95E+03	78.91	3.28	3.21	3.44	1.02E-12	1.04E-12	9.74E-13	8.95E-09	9.21E-09	8.38E-09
L8	39 - 56	49.93	9.27E+02	80.63	3.44	3.76	4.06	6.97E-13	6.37E-13	5.89E-13	5.33E-09	4.72E-09	4.24E-09
	43 - 55	47.82	1.33E+03	86.89	3.97	3.89	4.27	4.56E-13	4.65E-13	4.24E-13	3.00E-09	3.08E-09	2.72E-09
	41 - 55	46.59	1.61E+03	90.68	4.14	3.81	4.79	3.71E-13	4.03E-13	3.21E-13	2.27E-09	2.54E-09	1.86E-09
	39 - 53	45.40	4.93E+02	86.90	3.98	3.63	4.62	3.89E-13	4.26E-13	3.35E-13	2.43E-09	2.74E-09	1.98E-09
L10	45 - 55	49.63	2.93E+04	121.58	3.95	3.26	3.72	2.62E-13	3.17E-13	2.78E-13	1.42E-09	1.84E-09	1.53E-09
	44 - 55	50.31	3.07E+04	107.39	3.70	3.41	3.93	3.73E-13	4.05E-13	3.52E-13	2.29E-09	2.56E-09	2.11E-09
	43 - 54	48.79	3.07E+04	119.37	4.17	3.51	4.06	2.44E-13	2.90E-13	2.51E-13	1.29E-09	1.63E-09	1.34E-09
	39 - 48	43.72	1.56E+03	99.12	4.04	3.56	3.68	2.63E-13	2.99E-13	2.89E-13	1.43E-09	1.69E-09	1.62E-09
L18	46 - 57	50.50	8.87E+02	69.51	5.16	5.34	4.54	6.46E-13	6.23E-13	7.34E-13	4.81E-09	4.59E-09	5.72E-09
	42 - 55	47.31	1.78E+03	93.67	4.90	4.49	4.69	3.08E-13	3.36E-13	3.22E-13	1.77E-09	1.98E-09	1.87E-09
	49 - 59	58.12	4.74E+03	85.83	3.53	3.42	2.57	9.45E-13	9.74E-13	1.30E-12	8.04E-09	8.38E-09	1.23E-08
	43 - 55	48.34	1.33E+03	84.51	5.03	4.70	4.38	3.93E-13	4.21E-13	4.51E-13	2.46E-09	2.69E-09	2.96E-09

Table A.2 Full compilation of Discharge rates, decompression rates and fragmentation threshold.

ID	Discharge rate (Kg s^{-1})									Decompression rate (Mpa s^{-1})			ΔPfr (Mpa)		
	r_{25}	r_{25+}	r_{25-}	r_{50}	r_{50+}	r_{50-}	r_{100}	r_{100+}	r_{100-}	dP/dt	dP/dt +	dP/dt -	d1	d2	d3
L5	4.8E+07	3.4E+07	1.1E+08	1.9E+08	1.4E+08	4.3E+08	7.7E+08	5.4E+08	1.7E+09	0.51	0.36	1.13	4.28	4.28	4.23
	1.3E+08	9.3E+07	2.9E+08	5.3E+08	3.7E+08	1.2E+09	2.1E+09	1.5E+09	4.7E+09	1.38	0.97	3.08	4.24	4.28	4.21
	1.6E+08	1.1E+08	3.6E+08	6.5E+08	4.6E+08	1.4E+09	2.6E+09	1.8E+09	5.8E+09	1.70	1.19	3.79	4.32	4.50	4.45
	1.6E+08	1.1E+08	3.6E+08	6.4E+08	4.5E+08	1.4E+09	2.6E+09	1.8E+09	5.7E+09	1.68	1.18	3.75	4.28	4.43	4.39
L1	2.3E+08	1.6E+08	5.2E+08	9.3E+08	6.5E+08	2.1E+09	3.7E+09	2.6E+09	8.3E+09	2.43	1.71	5.43	4.79	4.74	4.68
	1.3E+08	8.8E+07	2.8E+08	5.0E+08	3.5E+08	1.1E+09	2.0E+09	1.4E+09	4.5E+09	1.31	0.92	2.93	5.64	5.65	5.62
	1.5E+08	1.1E+08	3.4E+08	6.2E+08	4.3E+08	1.4E+09	2.5E+09	1.7E+09	5.5E+09	1.62	1.13	3.61	5.48	5.45	5.41
	2.3E+08	1.6E+08	5.2E+08	9.3E+08	6.5E+08	2.1E+09	3.7E+09	2.6E+09	8.3E+09	2.43	1.71	5.43	4.79	4.74	4.68
L2	1.0E+08	7.2E+07	2.3E+08	4.1E+08	2.9E+08	9.2E+08	1.6E+09	1.2E+09	3.7E+09	1.08	0.75	2.40	4.32	4.42	4.36
	1.3E+08	8.8E+07	2.8E+08	5.0E+08	3.5E+08	1.1E+09	2.0E+09	1.4E+09	4.5E+09	1.31	0.92	2.93	4.26	4.35	4.27
	5.2E+07	3.6E+07	1.2E+08	2.1E+08	1.5E+08	4.6E+08	8.3E+08	5.8E+08	1.8E+09	0.54	0.38	1.21	4.47	4.52	4.49
	4.1E+07	2.9E+07	9.2E+07	1.6E+08	1.2E+08	3.7E+08	6.6E+08	4.6E+08	1.5E+09	0.43	0.30	0.96	4.37	4.45	4.45
L3	1.2E+08	8.7E+07	2.8E+08	5.0E+08	3.5E+08	1.1E+09	2.0E+09	1.4E+09	4.4E+09	1.30	0.91	2.91	4.01	3.93	4.02
	1.4E+08	9.5E+07	3.0E+08	5.4E+08	3.8E+08	1.2E+09	2.2E+09	1.5E+09	4.8E+09	1.42	1.00	3.17	4.29	4.29	4.42
	9.6E+07	6.7E+07	2.1E+08	3.8E+08	2.7E+08	8.6E+08	1.5E+09	1.1E+09	3.4E+09	1.01	0.71	2.24	3.93	4.00	4.07
	6.2E+07	4.4E+07	1.4E+08	2.5E+08	1.8E+08	5.6E+08	1.0E+09	7.0E+08	2.2E+09	0.65	0.46	1.46	4.31	4.34	4.39
L4	2.7E+08	1.9E+08	6.0E+08	1.1E+09	7.5E+08	2.4E+09	4.3E+09	3.0E+09	9.6E+09	2.80	1.96	6.25	4.05	4.02	4.01
	7.3E+07	5.1E+07	1.6E+08	2.9E+08	2.1E+08	6.5E+08	1.2E+09	8.2E+08	2.6E+09	0.76	0.54	1.71	4.22	4.21	4.18
	8.2E+07	5.8E+07	1.8E+08	3.3E+08	2.3E+08	7.3E+08	1.3E+09	9.2E+08	2.9E+09	0.86	0.60	1.92	4.13	4.07	4.07
	9.0E+07	6.3E+07	2.0E+08	3.6E+08	2.5E+08	8.0E+08	1.4E+09	1.0E+09	3.2E+09	0.94	0.66	2.10	4.14	4.08	4.10

ID	Discharge rate (Kg s^{-1})									Decompression rate (Mpa s^{-1})			ΔPfr (Mpa)		
	r_{25}	r_{25+}	r_{25-}	r_{50}	r_{50+}	r_{50-}	r_{100}	r_{100+}	r_{100-}	dP/dt	dP/dt +	dP/dt -	d1	d2	d3
L12	2.6E+08	1.8E+08	5.8E+08	1.0E+09	7.4E+08	2.3E+09	4.2E+09	2.9E+09	9.4E+09	2.74	1.92	6.12	3.68	3.68	3.64
	1.5E+08	1.1E+08	3.4E+08	6.1E+08	4.3E+08	1.4E+09	2.4E+09	1.7E+09	5.5E+09	1.60	1.12	3.57	3.76	3.70	3.66
	2.2E+08	1.6E+08	5.0E+08	8.9E+08	6.2E+08	2.0E+09	3.6E+09	2.5E+09	7.9E+09	2.33	1.63	5.19	3.76	3.71	3.70
	4.3E+07	3.0E+07	9.5E+07	1.7E+08	1.2E+08	3.8E+08	6.8E+08	4.8E+08	1.5E+09	0.44	0.31	0.99	4.21	4.13	4.13
L6	1.8E+08	1.3E+08	4.0E+08	7.2E+08	5.0E+08	1.6E+09	2.9E+09	2.0E+09	6.4E+09	1.87	1.31	4.17	4.44	4.49	4.46
	3.3E+07	2.3E+07	7.4E+07	1.3E+08	9.3E+07	3.0E+08	5.3E+08	3.7E+08	1.2E+09	0.35	0.24	0.77	4.47	4.49	4.50
	1.3E+08	9.0E+07	2.9E+08	5.1E+08	3.6E+08	1.1E+09	2.0E+09	1.4E+09	4.6E+09	1.34	0.94	2.99	4.24	4.26	4.22
	1.5E+08	1.1E+08	3.4E+08	6.0E+08	4.2E+08	1.3E+09	2.4E+09	1.7E+09	5.4E+09	1.58	1.11	3.53	4.25	4.27	4.21
L8	3.1E+07	2.2E+07	6.9E+07	1.2E+08	8.7E+07	2.8E+08	5.0E+08	3.5E+08	1.1E+09	0.33	0.23	0.73	4.40	4.34	4.29
	4.0E+07	2.8E+07	8.8E+07	1.6E+08	1.1E+08	3.5E+08	6.3E+08	4.4E+08	1.4E+09	0.41	0.29	0.92	4.32	4.33	4.28
	4.5E+07	3.2E+07	1.0E+08	1.8E+08	1.3E+08	4.0E+08	7.2E+08	5.0E+08	1.6E+09	0.47	0.33	1.05	4.31	4.36	4.24
	2.0E+07	1.4E+07	4.6E+07	8.2E+07	5.7E+07	1.8E+08	3.3E+08	2.3E+08	7.3E+08	0.21	0.15	0.48	4.45	4.51	4.37
L10	3.1E+08	2.2E+08	6.9E+08	1.2E+09	8.7E+08	2.8E+09	5.0E+09	3.5E+09	1.1E+10	3.25	2.28	7.25	3.89	3.97	3.91
	3.2E+08	2.3E+08	7.2E+08	1.3E+09	9.0E+08	2.9E+09	5.1E+09	3.6E+09	1.1E+10	3.36	2.36	7.49	4.00	4.04	3.97
	3.2E+08	2.2E+08	7.1E+08	1.3E+09	9.0E+08	2.9E+09	5.1E+09	3.6E+09	1.1E+10	3.35	2.35	7.47	3.93	4.00	3.94
	4.4E+07	3.1E+07	9.8E+07	1.8E+08	1.2E+08	3.9E+08	7.0E+08	4.9E+08	1.6E+09	0.46	0.32	1.03	4.42	4.48	4.46
L18	3.0E+07	2.1E+07	6.7E+07	1.2E+08	8.5E+07	2.7E+08	4.8E+08	3.4E+08	1.1E+09	0.32	0.22	0.70	4.30	4.27	4.38
	4.8E+07	3.4E+07	1.1E+08	1.9E+08	1.3E+08	4.3E+08	7.7E+08	5.4E+08	1.7E+09	0.50	0.35	1.12	4.15	4.20	4.18
	9.2E+07	6.5E+07	2.1E+08	3.7E+08	2.6E+08	8.2E+08	1.5E+09	1.0E+09	3.3E+09	0.96	0.68	2.15	3.97	3.99	4.21
	4.0E+07	2.8E+07	8.8E+07	1.6E+08	1.1E+08	3.5E+08	6.3E+08	4.4E+08	1.4E+09	0.41	0.29	0.92	4.19	4.23	4.26

A.3 TauFactor reports sample for L4

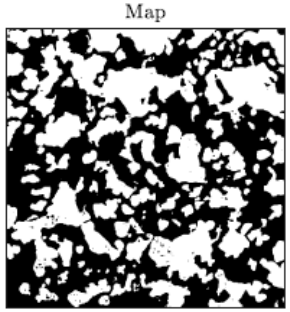

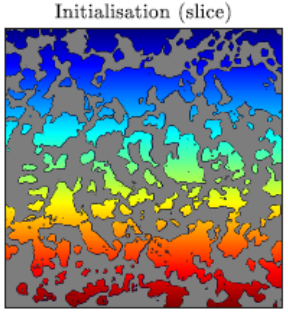

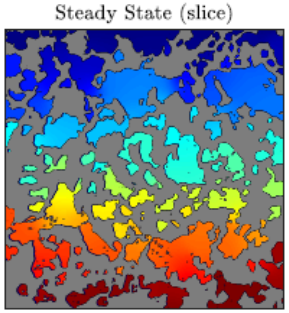

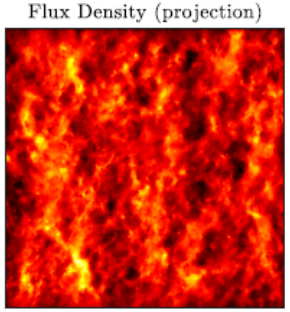

$$D^{\text{eff}} = D\frac{\varepsilon}{\tau^*}$$

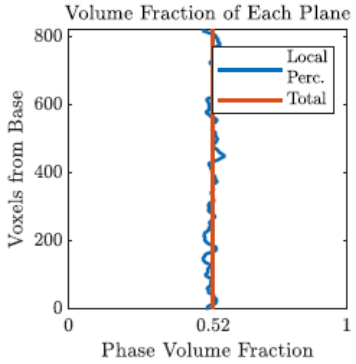

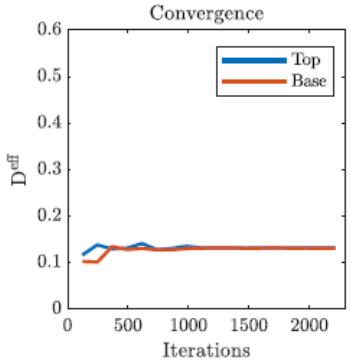

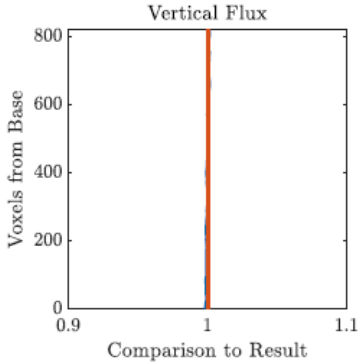

Voxel volume: 820×820×820
Voxel size (nm): 1300×1300×1300
Sample size (μm): 1070×1070×1070
Direction 1
Phase White

D^{eff} (m^2s^{-1}) = 0.131
Tortuosity factor = 3.96

Phase volume fraction = 51.8%
Directional percolation = 100%

Number of iterations = 2214
Simulation = 85 min